Atomistic simulations of liquid–liquid coexistence in confinement: comparison of thermodynamics and kinetics with bulk

Subir K. Das

Taylor & Francis
Taylor & Francis Group

CONFINED FLUIDS

Atomistic simulations of liquid–liquid coexistence in confinement: comparison of thermodynamics and kinetics with bulk

Subir K. Das*

Theoretical Sciences Unit, Jawaharlal Nehru Centre for Advanced Scientific Research, Jakkur, Bangalore 560064, India

We review a few simulation methods and results related to the structure and non-equilibrium dynamics in the coexistence region of immiscible symmetric binary fluids, in bulk as well as under confinement, with special emphasis on the latter. Monte Carlo methods to estimate interfacial tensions for flat and curved interfaces have been discussed. The latter, combined with a thermodynamic integration technique, provides contact angles for coexisting fluids attached to the wall. For such three-phase coexistence, results for the line tension are also presented. For the kinetics of phase separation, various mechanisms and corresponding theoretical expectations have been discussed. A comparative picture between the domain growth in bulk and confinement (including thin-film and semi-infinite geometry) has been presented from molecular dynamics simulations. Applications of finite-size scaling technique have been discussed in both equilibrium and non-equilibrium contexts.

Keywords: interfacial tension; line tension; contact angle; nucleation; wetting; Young's equation; kinetics of phase separation; surface-directed spinodal decomposition; Monte Carlo; molecular dynamics; finite-size scaling

1. Introduction

Topics related to phase transitions and coexistence, both in equilibrium [1–31] and non-equilibrium [32–60] contexts, attracted substantial interest over many decades. Despite significant activities, challenges remain, both in bulk and under confinement, particularly related to nucleation and growth. These are of much recent interest.[61–124] There exist, of course, analytical theories that address intriguing questions in this area. However, often these theories, particularly for fluids, are simple (though elegant) scaling arguments or are inaccurate due to, e.g., being of mean field nature, lacking fluctuations, and therefore require verification. Computer simulations of simple but physically motivated statistical mechanical models have been successful in guiding some of the theories, thus providing improved understanding. Our aim here is to discuss Monte Carlo (MC) [125–127] and molecular dynamics (MD) [126,127] methods and results obtained via these simulations, relevant in this context, with a comparative picture between bulk and confined fluids, both in equilibrium and non-equilibrium scenarios.

Phase diagram of a normal chemical system is schematically shown in Figure 1(a), in pressure (*P*) versus temperature (*T*) plane. Along various continuous lines two different phases coexist with each other in equilibrium. Three-phase coexistence occurs at the meeting point of all three coexistence curves. A first-order phase transition [2,7] takes place when we move from one equilibrium phase to the other, crossing any of these lines. The relevant order parameter, in this case density (ρ), then exhibits a jump. The vapour–liquid coexistence curve terminates at the critical point (C) where a transition between these two phases is not accompanied by an order-parameter jump. [2,7] This is referred to as a continuous or second-order phase transition.[2–5]

The vapour–liquid coexistence curve in $T-\rho$ plane has been schematically shown in Figure 1(b) where the left branch corresponds to the low-density vapour phase and the right branch is for the high-density liquid phase. Analogous curve can be drawn for the coexistence between two components in an immiscible $A + B$ system, by replacing ρ by x_s ($= N_s/N$, where N_s and N are, respectively, the number of s and total particles), the concentration of species s. For $s = A$, the left branch corresponds to the concentration of A particles in the B-rich phase and right branch to that in the A-rich phase. The above-depicted phase behaviour is for the bulk system. Corresponding diagram for a confined system [55] is far more complex which is briefly touched upon later.

Nucleation and growth [10–20] are at the core of coexistence phenomena. Knowledge of interfacial tension is crucial to the understanding of those. For nucleations to occur in any phase transition, the system needs to
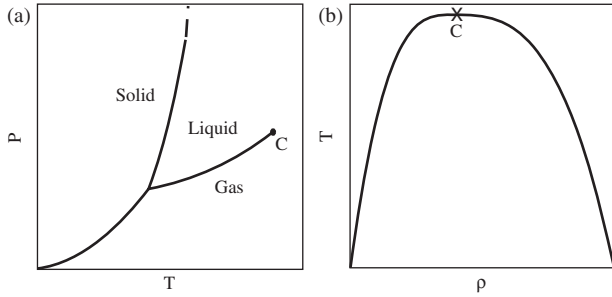
*Email: das@jncasr.ac.in

Figure 1.   (a) Schematic phase diagram of a normal chemical system in pressure versus temperature plane. Various phases and coexistence curves separating them are shown. The vapour–liquid coexistence line terminates at a critical point (C). (b) A schematic vapour–liquid coexistence curve is shown in temperature versus density plane.

overcome the barrier originating from the competition between the bulk and interfacial free energies. For a spherical (space dimension $d = 3$) nucleus, this can be obtained from the maximum of

$$\Delta F(R) = -\frac{4}{3}\pi R^3 f_b + 4\pi R^2 \gamma, \qquad (1)$$

where f_b is the bulk free energy density, γ is the interfacial tension and R is the radius of the nucleus or droplet. Depending upon the supersaturation, i.e., proximity to the coexistence curve, nucleations may be rare events. Usually the size of a droplet at the maximum of ΔF is nanoscopic, thus having strong curvature. This latter fact is traditionally ignored and for γ, values from flat interfaces ($R \rightarrow \infty$) are used. In heterogeneous nucleation, say, in the presence of a wall with favourable wetting [21–31] condition, the nucleation barrier gets reduced. To study this, in addition to the information on curvature dependence of γ, we need accurate knowledge of other quantities, e.g., contact angle and line tension.[27,28]

A schematic picture of a coexisting binary fluid, confined between two parallel walls, separated by distance
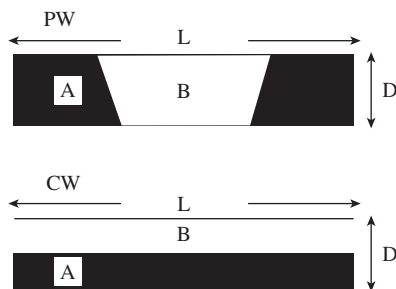

Figure 2.   Schematic demonstration of partial (PW) and complete (CW) wettings when an immiscible binary mixture $(A + B)$ is confined between anti-symmetric walls. The upper wall prefers B particles and the lower prefers A particles. The contact angle θ is the angle made by the AB interface with the wall. For the CW case, θ is zero.

D, is shown in Figure 2. For the sake of brevity, we have demonstrated only the case with anti-symmetric walls where one (lower) wall prefers A and the other B. For the symmetric case, both the walls will be richer in the same (preferred) component. Partially (PW) and completely wet (CW) states are shown which will be formally defined soon. The line tension comes from the region where the interface of AB coexistence meets a wall. This can be appreciated from a $3 - d$ picture. For simplicity, we avoided drawing curved interfaces.

Among other examples, confined systems are relevant in the context of porous media. Thus, from technological point of view, applications are widespread, e.g., recovery of oil from porous rocks and nanofluidic devices. These involve nanoscopic pores and phenomena related to wetting or drying, associated with curved interfaces, which are, as discussed, of fundamental scientific interest.

In kinetics, however, after stable droplets, from homogeneous or heterogeneous condition, following quench in relevant thermodynamic variables, have formed, the primary interest is to learn the time dependence of the size of droplets, as the system approaches equilibrium. [32–39,55] In the case of fluids, even deep inside the coexistence region (spinodal regime), where the systems fall unstable instantaneously, the kinetics is rather complex. There multiple scaling regimes for the time dependence of the characteristic length scale exist, making the problem challenging even in the bulk, particularly from the simulation point of view. In confinement, complexities related to wetting or drying bring additional challenges both theoretically and computationally. For example, due to the competition with phase separation at the interior of the film, the kinetics of wetting at the walls can be non-monotonic.[112] This is illustrated in Figure 3,
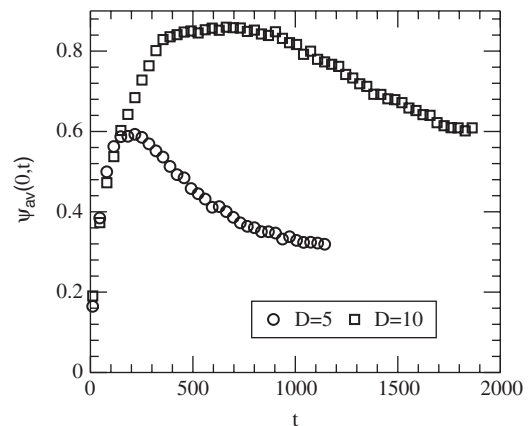

Figure 3.   Plots of average order-parameter at the walls of symmetric thin films (both walls prefer A particles) versus time. These plots were obtained from MD simulations of a binary LJ fluid which will be defined later. Results are presented for two different thicknesses $D = 5$ and 10. From Phys. Rev. E **73**, 031604 (2006).

where we show plots of the order-parameter value at the walls, from MD simulations of a model binary fluid (defined later) confined between two symmetric parallel walls, with the increase of time, for two different thicknesses D. From the trend at early time, we may mistakenly conclude that the preferred component is going to completely wet the wall. But this is not true and is appreciable from the decay at late time. Thus, for a complete understanding of the kinetics under confinement, knowledge of equilibrium, in this case of wetting transition, is needed via independent studies. For quantification of growth in general, in bulk or under confinement, information about equilibrium transport properties also becomes essential. This, of course, is expected and will be clear later. These are various viscosities and diffusivities.

The objective of the article is to review the status of computational methodologies using which studies of the above-mentioned challenging issues of modern statistical mechanics, concerning both equilibrium and non-equilibrium, are possible, via atomistic models for fluids. In computer simulations, the transport properties of a fluid can be calculated from the standard Green–Kubo or Einstein relations.[128] These we do not discuss here. In this article, we focus on the interfacial tension, contact angle, line tension, etc., in addition to kinetics of phase transitions. Primary focus though is in confinement, the bulk properties are touched upon as necessity as well as to bring completeness. Throughout the article, we use symmetric binary fluid mixtures. In addition to technical advantages, such symmetries are useful in analysis of data as well.

The rest of the article is organised as follows. In Section 2, we discuss equilibrium phenomena. There we present methods to obtain phase behaviour and interfacial tensions in bulk. In confinement, reduction of nucleation barrier with respect to the bulk is demonstrated via state-of-the-art calculation of contact angle. Relevance of line tension is discussed in this context. Non-equilibrium issues are presented in Section 3. There, though we discuss the case of droplet nucleation and growth, results are presented, for both bulk and confinement, only for compositions of A and B particles deep inside the coexistence curve. Section 4 concludes the article with a brief summary and outlook.

2.   Equilibrium aspects of phase coexistence

In the vicinity of a critical point, various thermodynamic and transport properties exhibit power law singularities. This critical phenomena [5,125] is primarily characterised by the diverging correlation length (ξ) and relaxation time (τ). In the following, we briefly describe the behaviour of a few static quantities for a binary mixture. The order parameter m ($= x_A - x_A^c$, x_A^c being the critical value of the concentration), ξ and interfacial tension (γ) behave as

$$m \approx \hat{B}\epsilon^{\beta}, \tag{2}$$

$$\xi \approx \xi_0^{\pm}\epsilon^{-\nu}, \tag{3}$$

$$\gamma \approx \gamma_0\epsilon^{(d-1)\nu}, \tag{4}$$

where $\epsilon = |T - T_c|/T_c$, T_c being the critical temperature, and the superscripts on the amplitude ξ_0 are indicative of the presence of singularities irrespective of from which side of T_c we approach it. The values of the critical exponents are universal irrespective of the type of material and transition. For example, the exponents are same for vapour–liquid, liquid–liquid or a demixing critical transition in a solid binary mixture. Renormalisation group theory helped understand [4,5,9] such universalities where the basic essence is that the microscopic details for such large length scale phenomena is unimportant. The objective of this article, by no means, is to provide detailed discussion on critical phenomena. For different universality classes, based on order-parameter components, system dimensionality and range of interaction, the readers are referred to existing reviews in the literature. [5,8,9] Here, we only mention that the values of the above-mentioned exponents in $d = 3$ Ising (short-range) universality class are [9] $\beta \simeq 0.325$ and $\nu \simeq 0.629$. Such universalities exist in kinetics of phase transition as well. This is, however, more complex and less robust in fluids compared to phase separation in solid binary mixtures. We discuss it in detail later.

Confinement reduces the critical temperature.[21] The deviation, ΔT, of the critical temperature, from the thermodynamic limit value, scales with D as [21,125, 129–131]

$$\Delta T \sim D^{-1/\nu}. \tag{5}$$

In addition to this, when preferential attraction for one of the components is switched on, the composition in the interior of the film no longer remains symmetric, thus the phase diagram becomes (more) asymmetric with respect to the critical point.[55] Due to the restriction of growth of ξ in the direction perpendicular to the walls, it is expected that the critical exponents will belong to the $2 - d$ universality class.

For phase separation in confinement, the basic Young's equation connects three interfacial tensions and contact angle θ as [17,55]

$$\gamma \cos \theta = \gamma_{WA} - \gamma_{WB}, \tag{6}$$

where γ_{WA} (γ_{WB}) is the interfacial tension of the wall with A (B)-rich phase and γ is that for the AB interface. Situation becomes even more involved when interfaces are

curved and line tension (introduced later) becomes important. Depending upon the wall particle interaction range, the wetting transition can have different orders.[21] Those issues are not touched here.

In the following, we define models for the bulk as well as for confinement. In some cases, slightly different versions are adopted which we point out in appropriate places.

2.1 Model

We choose a model binary mixture, [132–135] where the particles of equal mass (m_p) and diameter (σ), at distance r apart, interact with each other via ($r_c = 2.5\sigma$)

$$U_{sv}(r < r_c) = u_{sv}(r) - u_{sv}(r_c) - (r - r_c)$$
$$\times \frac{du_{sv}(r)}{dr}\bigg|_{r=r_c}, \quad U_{sv}(r \geq r_c) = 0, \quad (7)$$

where

$$u_{sv}(r) = 4\varepsilon_{sv}\left[\left(\frac{\sigma}{r}\right)^{12} - \left(\frac{\sigma}{r}\right)^6\right] \quad (8)$$

is the standard Lennard-Jones (LJ) potential. The last term on the right hand side of the first part of Equation (7) is introduced for the purpose of making the force smooth at $r = r_c$ where the original LJ potential is cut and shifted to zero. For the choice of the interaction strengths $\varepsilon_{AA} = \varepsilon_{BB} = 2\varepsilon_{AB} = \varepsilon = 1$, we have a perfectly symmetric phase separating model for which $x_A^c = 1/2$. We work with a high-density ρ (= $N/V = 1$, in case of bulk fluid $V = L^3$, L being the linear dimension of a periodic cubic box in units of σ) to avoid overlap with a liquid–gas transition.

For the study of wetting, we put our binary mixture between two parallel walls which interact with A particles via [83,84]

$$u_A(z) = \frac{2\pi\rho}{3}\left\{\varepsilon_r\left[\left(\frac{\sigma}{z + z_0}\right)^9 + \left(\frac{\sigma}{D + z_0 - z}\right)^9\right]\right.$$
$$\left. - \varepsilon_a\left(\frac{\sigma}{z + z_0}\right)^3\right\}, \quad (9)$$

and with B particles via

$$u_B(z) = \frac{2\pi\rho}{3}\left\{\varepsilon_r\left[\left(\frac{\sigma}{z + z_0}\right)^9 + \left(\frac{\sigma}{D + z_0 - z}\right)^9\right]\right.$$
$$\left. - \varepsilon_a\left(\frac{\sigma}{D + z_0 - z}\right)^3\right\}, \quad (10)$$

where $0 \leq z \leq D$ is the coordinate in the direction perpendicular to the walls. In this case, we have periodic boundary conditions only in x and y directions, and the corresponding linear dimension is represented by L. In Equations (9) and (10), $z_0 = \sigma/2$ and is chosen to ensure that the wall potentials do not diverge within the width of the film. In order to work with the smooth walls, various parts in these potentials are obtained by integrating the LJ potential under semi-infinite approximation. There ε_r and ε_a, both being positive, correspond respectively to repulsion and attraction. It is clear that both the walls repel A and B particles with equal strength whereas the lower wall attracts A and the upper wall prefers B. This antisymmetric design was chosen for reasons to become clear soon.

As mentioned in the previous section, the methods that we discuss in the context of confinement, to a significant extent, are complemented by some in bulk. Also, without a discussion of the bulk phenomena, the problems under confinement will not be completely appreciated. Thus, for the sake of convenience, first we present the case of bulk coexistence.

2.2 Bulk coexistence

The phase behaviour and interfacial tensions for a liquid–liquid transition can be conveniently and accurately obtained via MC simulations in semi-grand canonical ensemble (SGMC).[125,126] In this ensemble, in addition to the standard displacement moves, we allow identity switches $A \rightarrow B \rightarrow A$ such that there is fluctuation of x_s during the simulation. Such identity moves require the difference between the chemical potentials of the two species to be contained in the Boltzmann factor. For the present model, due to the symmetry, this difference is zero along coexistence.

For the sake of brevity, we provide only a brief description of the Metropolis algorithm,[125,126] related to MC technique. In each trial move, the energy difference between the new and old states is calculated. This is used in the computation of the Boltzmann factor which is then compared with a random number between 0 and 1. If the Boltzmann factor is greater than the random number, the new state is accepted. Otherwise, the system resides in the original state.

From the fluctuations of x_s, we can obtain the probability distributions $P_L(x_s)$, the subscript L being used because of the finite-size effects. Below T_c, $P_L(x_s)$ will have a two peak structure and above it there will be a single peak in the distribution. Figure 4(a) shows two plots of $P_L(x_A)$, versus x_A, one in the coexistence region ($T < T_c$) and the other at homogeneous region ($T > T_c$). For $T < T_c$, the locations of the peaks provide the coexistence curve. The two peaks, as the temperature increases from the lower side of T_c, should merge at T_c. However, this ideal situation occurs only for $L = \infty$. For
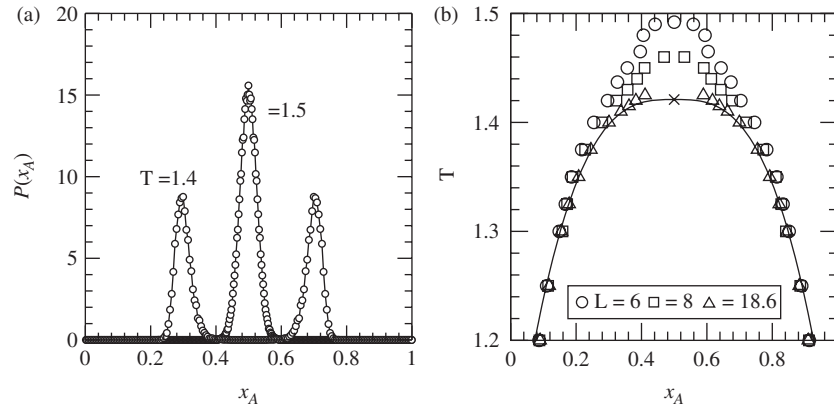
Figure 4.   (a) Probability distribution $P(x_A)$, obtained from the fluctuations of A particles in the SGMC simulations of the symmetric binary LJ model in bulk, is plotted versus x_A. The temperatures are mentioned on the figure. For both the temperatures, total number of particles used was $N = 6400$. The distributions were symmetrised by using the fact $P(x_A) = P(1 - x_A)$, having its root in the model symmetry. (b) (Reproduced with permission from J. Chem. Phys. **139**, 064505 (2013). Copyright 2013, AIP Publishing LLC.) Bulk coexistence curves for the symmetric LJ model, obtained from SGMC simulations, for a few different system sizes L, as indicated on the figure. The continuous line is a fit to the data-set for largest system size, using only the region unaffected by finite size of the system, to the critical form of the order parameter in Equation (2). The value of β was fixed to the $d = 3$ Ising value.

$L < \infty$ there are finite-size effects in the phase diagram. [125,129,130] This is shown [134,135] in Figure 4(b) where we have plotted coexistence curves from few different system sizes. This allows us to define the finite-size critical point, T_c^L, as the temperature, where $P_L(x_s)$ exhibits a transition between unimodal and bimodal structures. The finite-size scaling behaviour of T_c^L should have a form [125,129,130] similar to Equation (5), i.e.,

$$T_c^L - T_c \sim L^{-1/\nu}, \tag{11}$$

which can be appreciated from Equation (3). By fixing ν to the value of the expected universality class, T_c can be obtained from Equation (11) when we have simulation results from multiple system sizes. There are other ways of obtaining T_c as well which we discuss below.

We can obtain T_c by judicially choosing the order parameter versus temperature data from a region unaffected by finite value of L and fitting those to the form of the order parameter given in Equation (2). In this method also, of course, we fix the value of β to the expected universality class. An unbiased method involves the crossing of temperature-dependent data for Binder parameter (BP) [125] from different system sizes. With this latter technique, a better estimate requires the knowledge of finite-size scaling behaviour of the BP. For the sake of brevity, we do not discuss the method of BP intersection here. However, finite-size scaling technique, in a rather general context, for critical singularities is briefly introduced in the following. Before moving to that, we mention that the T_c for the above-mentioned model was obtained [134,135] to be 1.421 ε/k_B, k_B being the Boltzmann constant (from here on ε/k_B will be set to unity), and estimates from various different methods

[132,133] agreed with each other within small numerical error.

Noting that at the criticality the system size scales with ξ, we can write the finite-size scaling form of a quantity X, exhibiting critical singularity with exponent x, as [125]

$$X = L^{-x/\nu} Y(y); \quad y = \left(\frac{L}{\xi}\right)^{1/\nu}, \tag{12}$$

where the scaling function Y, independent of the system size, will have a near constant behaviour close to the criticality. Far away from criticality ($y \gg 1$), where there are no size effects, dependence of Y on y should be such that the thermodynamic limit form of X is recovered. This is possible when

$$Y \sim y^x. \tag{13}$$

This fact has been extensively used in the literature to obtain various critical exponents, using simulation data from finite systems. For an appropriate choice of the exponent, the system size independence of Y will be realised. Even though we do not use it in this article in the equilibrium context, the introduction of this scaling analysis here will be useful when we define and apply it in non-equilibrium problem in the next section.

The interfacial free energy density can be obtained from the distribution $P_L(x_A)$ as [62,64,68–70,79,81,82]

$$f_L(x_A) = -\frac{1}{L^3} k_B T \ln \frac{P_L(x_A)}{P_L(x_A^{\text{coex}})}, \tag{14}$$

x_A^{coex} being the bulk coexistence composition of A particles in A (or B)-rich phase. The probability at this composition in Equation (14) is used to shift the minima of $f_L(x_A)$ to
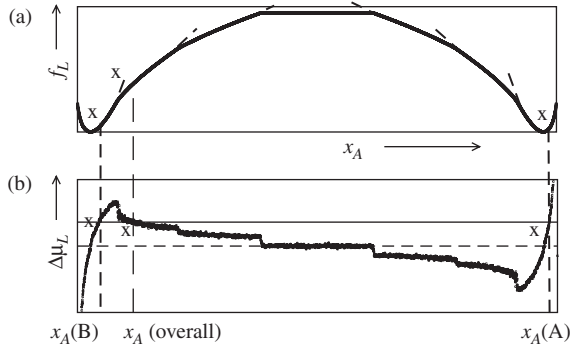
Figure 5. (a) Free energy density f_L, obtained from successive umbrella sampling SGMC simulations of the bulk LJ mixture, is plotted versus x_A. The various dashed lines are drawn to show sharp changes in slope, indicating structural changes from sphere to cylinder to slab, etc. The curve is symmetric about x_A^c, thus structures to be observed on the left side for A particles will get replaced by corresponding ones for B particles on the right. (b) Chemical potential $\Delta\mu_L$ is plotted versus x_A. Extraction of interfacial free energy from the combination of f_L and $\Delta\mu_L$ plots is demonstrated. For a overall composition x_A(overall) (in this case, at this composition a spherical droplet of A particles exist in the background of B-rich phase), chemical potential helps identify the concentrations of A and B particles in coexisting $A-$ and $B-$ rich phases. The free energies at all these concentrations can be read out to calculate the interfacial contribution for the spherical droplet. We do not mention the system size since the picture is being used for schematic explanation.

zero. A plot of f_L, as a function of x_A, is shown in Figure 5 (a). While the minima correspond to bulk coexisting phases, the maximum around x_A^c is due to the contribution from the interfaces. Thus the height of the maximum will provide the interfacial tension as [62]

$$\gamma(L) = \frac{L}{2} f_L(x_A^c), \qquad (15)$$

where the factor $1/2$ comes due to two equivalent interfaces that form under the periodic boundary conditions. This interfacial tension corresponds to the situation when we have slab-like structure of the

coexisting phases, giving rise to flat interfaces which classical nucleation theory (CNT) [11,12,17,19,22,23] deals with, even for nanoscopic droplet structure with strong curvature.

Here it must be mentioned that with standard SGMC simulations at low enough temperatures, it may not be possible to sample the whole composition space due to high interfacial energy barrier between the coexisting phases. To avoid such difficulty, we have used the successive umbrella sampling [136] technique. Using this technique, it is possible to control the concentration of a species in such a way that in the coexisting situation various possible structures (sphere, cylinder and slab), shown in Figure 6, can be realised.[69] In fact a transition from one such structure to the other comes via sharp changes in slope in the free energy plot (see Figure 5). This can be better appreciated from the jumps in the chemical potential [64]

$$\frac{1}{k_\text{B}T}\Delta\mu_L(x_A) = \left[\frac{\partial f_L(x_A, T)}{\partial x_A}\right]_T, \qquad (16)$$

relative to the bulk coexistence. This is shown in Figure 5 (b) using real simulation data. To obtain information on the curvature dependence of interfacial tension, we should focus on the region of f_L, where the structure contains curved interface, i.e., the minority species forms either spherical or cylindrical droplets. Even though both these structures are suitable for obtaining the information on curvature dependence, we present results only from the analysis of spherical droplets [from the region between the first and second jumps in Figure 5(b)].

The basic principle [64] that needs to be followed here is that two phases coexist under equal chemical potential condition. This allows us to identify the compositions for the A-rich and B-rich coexisting phases for an overall given composition, represented by $x_A(A)$, $x_A(B)$ and x_A(overall), respectively, in Figure 5. Remaining task is to identify the volumes and free energy contributions for each of these phases. Sum of the two values of free energy
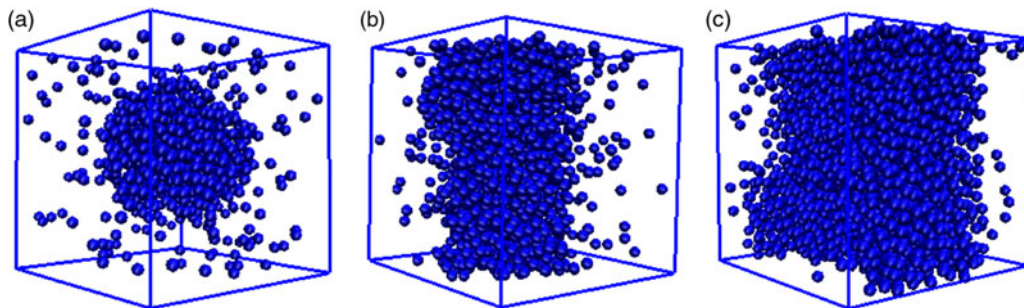

Figure 6. (Colour online) Various structures obtained for A particles from umbrella sampling SGMC simulations at $T = 1$ with $L = 18$. B particles are unmarked. The concentrations in (a), (b) and (c) are $x_A = 0.15$ (sphere), 0.27 (cylinder) and 0.5 (slab). From Phys. Rev. E **84**, 061607 (2011).
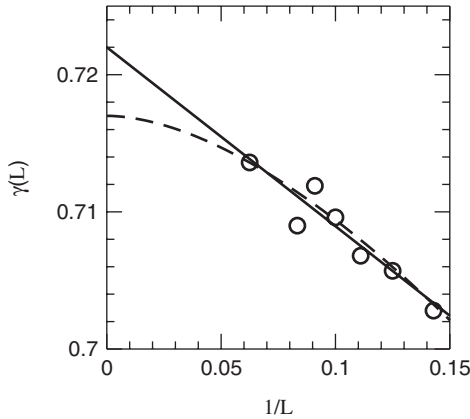
Figure 7. Plot of system size-dependent flat interfacial tension $\gamma(L)$ as a function of $1/L$ at $T = 1$. The solid line is a linear extrapolation to obtain $\gamma(\infty) = \gamma$. The dashed line has a form $\gamma(L) = \gamma + a_0 x^2 \ln b_0 x$; $x = 1/L$.

at $x_A(A)$ and $x_A(B)$ should be subtracted from the total value at x_A(overall), all of them being readable from f_L versus x_A plot, to obtain the interfacial contribution, F_s. With the reasonable approximation that the structure of droplet is spherical, radius R can be obtained from the volume of the minority phase. The latter is straightforward once the overall composition and that of the coexisting phases are read out. Then

$$\gamma(R) = \frac{F_s(R)}{4\pi R^2}. \tag{17}$$

In the limit $R \to \infty$, $\gamma(R)$ should tend to the flat interfacial tension $\gamma(L = \infty) = \gamma$. Here note that, as the argument suggests, $\gamma(L)$ also suffers from the finite-size effects due to suppression of fluctuations coming from inter-interface interaction in finite periodic boxes. So the data for multiple values of L should be obtained for a

meaningful extrapolation to $L \to \infty$ to estimate γ. This is demonstrated in Figure 7. There the solid line is a linear extrapolation in $1/L$ to obtain γ. A more recent study, however, convincingly showed a different functional form [91,92]

$$\gamma(L) \sim \frac{\ln L}{L^2}, \tag{18}$$

for the finite-size behaviour. The dashed line in Figure 7 represents a nice fit to the above-mentioned form. It is seen that for the present data-set the difference between the γ values obtained from these two different extrapolations is minor.

The size effects related to the finite value of R is different from that of $\gamma(L)$, since R-dependence is related to the shape. In Figure 8(a), we show plots [69] of $\gamma/\gamma(R) - 1$, with the variation of $1/R^2$, for different temperatures. The range of droplet size is restricted by the system size, thus data from different values of L are essential to explore a large range of R. Results from various values of L, for a particular temperature, in this figure, comply to a linear behaviour within statistical deviation. Thus, for the present model [69]

$$\gamma(R) = \frac{\gamma}{1 + 2(\ell_s/R)^2}. \tag{19}$$

The leading correction is quadratic due to the Ising-like particle–hole symmetry in the model. For such symmetric models, interchange of identities between the two phases should only change the sign of radius. Thus, corrections of odd order should not exist. For an asymmetric model, we expect linear correction as well, such that

$$\gamma(R) = \frac{\gamma}{1 + 2(\delta/R) + 2(\ell_s/R)^2}, \tag{20}$$
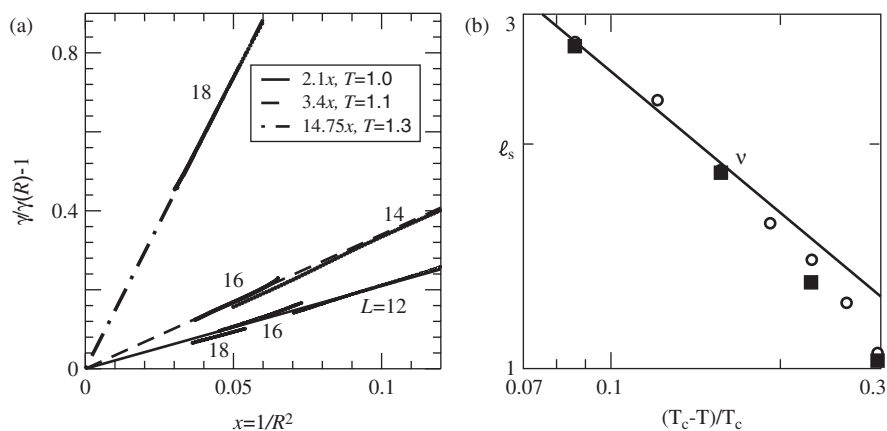

Figure 8. (a) Plots of $\gamma/\gamma(R) - 1$ versus $1/R^2$, at different temperatures. Data from various system sizes have been used. The solid straight lines provide an estimate for ℓ_s. In all the cases, values of γ used are obtained from the extrapolations via Equation (18). (b) Plot of ℓ_s versus ϵ. The continuous line has critical divergence $\sim t^{-\nu}$, ν having $d = 3$ Ising value. The open symbols correspond to linear extrapolations in $1/L$ to calculate γ from $\gamma(L)$ and the filled symbols were obtained by using Equation (18).

where δ is referred to as the Tolman length. [63,76,77,137–140] The value of ℓ_s can be obtained from Figure 8(a). Temperature dependence of this quantity is shown in Figure 8(b). Data obtained using γ from linear interpolation as well as via Equation (18) are included. There it is seen that [69]

$$\ell_s \sim \xi. \tag{21}$$

In asymmetric situation, Anisimov [63] predicted that

$$\delta \sim \xi^\phi; \quad \phi \simeq 1/2. \tag{22}$$

In Figure 9, we verify the critical behaviour of γ, as quoted in Equation (4). There also data for γ from linear extrapolation of $\gamma(L)$ in $1/L$ as well as from fitting to Equation (18) are used.

Combining Equation (19) with Equations (4) and (21), we obtain an universal critical behaviour of $\gamma(R)$, for a symmetric model, as [69]

$$\gamma(R)\xi^2 = \frac{C_1}{1 + C_2(\xi/R)^2}, \tag{23}$$

where the constants C_1 and C_2 are model independent. The value of C_2 is 32 which comes from the fact that [69] $\ell_s = 4\xi$. Furthermore, universality of C_1 can be appreciated from the amplitude ratio [8]

$$\omega = \frac{1}{4\pi\gamma_0(\xi_0^-)^2} \simeq 0.85, \tag{24}$$

providing $C_1 \simeq 0.094$. For the present model, this estimate of C_1 is lower by about 20% which is acceptable considering the complexities of simulation of atomistic fluids.

For temperatures close to T_c, the prediction in Equation (23) is valid irrespective of the presence or absence of the discussed symmetry in the model. This is because of the fact that the divergence of ℓ_s is much stronger than δ. Interesting observations of this type may not be possible for fluids under confinement, particularly with current status of simulation and analysis methods. There we deal with the methodologies for calculations of some basic quantities.

2.3 Confinement

In confined geometry, because of the additional interactions of the walls with A and B particles, situation is far more complex.[17,21–31,79,82–84,87] As encapsulated in Equation (6), there are now three interfacial tensions and a contact angle θ, formed where the AB interface meets a wall. Often it is possible that the wall has a preferential attraction for one of the components, say A, in the mixture. This will allow the A particles to wet the wall. This wetting can be complete or partial depending upon the wall–particle interaction and temperature. For non-preferential attraction, we have $\theta = 90°$ which decreases, when T is kept fixed, with the increase of strength of preference for A particles and eventually becomes zero at the wetting transition beyond which the wall is completely wet.

In Figure 10, we show snapshots from MC simulations in canonical ensemble for the model fluid confined between anti-symmetric walls described earlier.[83,84] In

Figure 10. Snapshots obtained from canonical ensemble MC simulations of the binary fluid confined between anti-symmetric walls (upper wall prefers B particles and lower A) at $T = 1$. The system dimensions are $L = 32$ and $D = 8$. Only A particles are shown in xz projection. The continuous lines are boundaries separating A- and B-rich phases. From Mol. Phys. **109**, 1043 (2011).
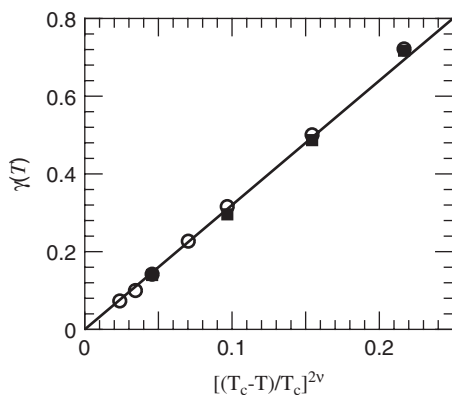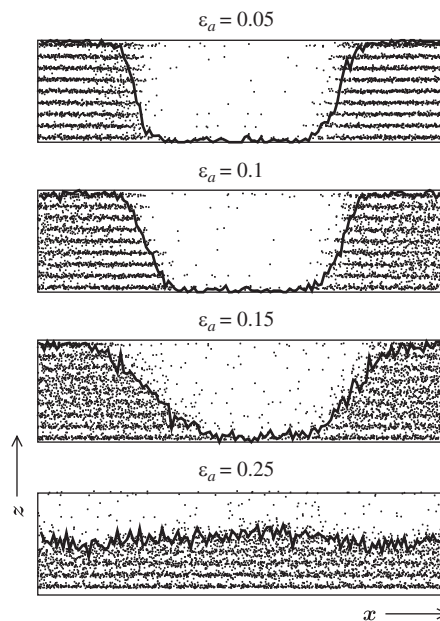

Figure 9. Critical behaviour of flat interfacial tension is confirmed. The opens symbols correspond to linear extrapolations using $\gamma(L)$ and the filled symbols are from extrapolations using Equation (18).

this ensemble, displacements of particles are the only allowed moves. Like in SGMC, these moves are accepted according to the standard Metropolis criterion. There it is seen that with the increase of ε_a the contact angle is decreasing, the last one representing a completely wet scenario. In computer simulations, traditional practice has been to estimate θ geometrically, demonstrated in Figure 10 where we can obtain θ from the slope of the continuous line, separating the A- and B-rich phases. While at temperatures far below the critical point this method may provide reasonably accurate estimates, at higher temperatures thermal fluctuations prevent us from drawing an accurate boundary between the above-mentioned two coexisting phases. Such difficulty can be avoided in appropriate thermodynamic method which we discuss in the following.[31,83,84]

The objective here is to obtain the difference $\gamma_{WA} - \gamma_{WB}$ which we aim to get via the SGMC simulations of the film described earlier. Based on the starting configuration, a 'simple' SGMC simulation will produce either a bulk A-rich or a bulk B-rich phase with wetting layers at preferred walls. In each of the cases, ε_a-dependent density profiles $\langle \rho_A(z) \rangle$ and $\langle \rho_B(z) \rangle$, averaged over x and y directions, can be obtained across the films. For $\varepsilon_a = 0$, these profiles will be symmetric around $z = D/2$ and asymmetry will be developed for $\varepsilon_a \neq 0$, as seen in Figure 11(a).

The total free energy of the system is

$$F = L^2 D f_b + L^2 \left(f_s^{z=0}(\varepsilon_a) + f_s^{z=D}(\varepsilon_a) \right), \quad (25)$$

where f_b is the bulk free energy density, $f_s^{z=0}$ is the corresponding density for the wall at $z = 0$ and $f_s^{z=D}$ is that for the wall at $z = D$. Involving one particular wall, the difference in interfacial tension can be written as

$$\gamma_{WA} - \gamma_{WB} = f_s^{z=0}(\varepsilon_a)|_{A-\text{rich}} - f_s^{z=0}(\varepsilon_a)|_{B-\text{rich}}. \quad (26)$$

This would require, of course, snapshots with A- and B-rich bulk phases. Given the symmetry of the model,

$$f_s^{z=0}(\varepsilon_a)|_{B-\text{rich}} = f_s^{z=D}(\varepsilon_a)|_{A-\text{rich}}, \quad (27)$$

providing

$$\gamma_{WA} - \gamma_{WB} = f_s^{z=0}(\varepsilon_a)|_{A-\text{rich}} - f_s^{z=D}(\varepsilon_a)|_{A-\text{rich}}, \quad (28)$$

conveniently allowing us to work with only one type of configurations, either A-rich or B-rich.

The total free energy

$$F = -k_B T \ln Z, \quad (29)$$

can be obtained from the partition function

$$Z \propto \int d\vec{X} \exp\left\{ -\frac{1}{k_B T}(H_b + H_r + H_a) \right\}, \quad (30)$$

where $\vec{X}$ represents degrees of freedom for all the configurations, and H_b, H_r and H_a are respectively the bulk, repulsive wall and attractive wall interaction contributions to the Hamiltonian, with
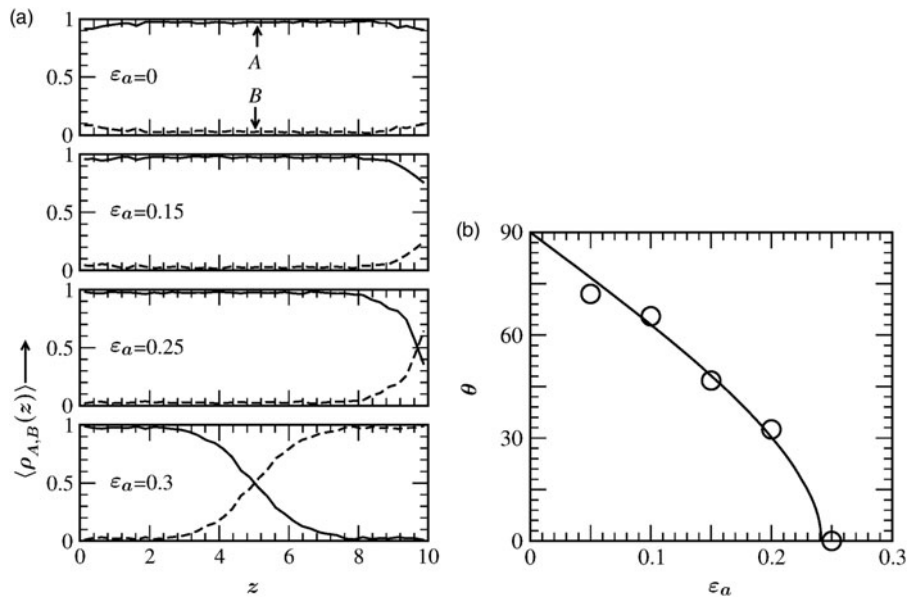

Figure 11. (a) Average density profiles $\langle \rho_s(z) \rangle$ as a function of z at $T = 1$, obtained from simple SGMC simulations of $A + B$ mixtures confined between anti-symmetric walls. Four different values of ε_a are included. (b) Contact angle θ obtained for the confined fluid at $T = 1$ is plotted versus ε_a. Results from both canonical (symbols) simulations (using geometric method) and SGMC (line) simulations (using thermodynamic method) are included. From EPL **92**, 26006 (2010).

$$H_a = \varepsilon_a L^2 \left(\frac{2\pi\rho}{3}\right)\left[\int_0^D \langle\rho_A(z)\rangle\left(\frac{\sigma}{z+z_0}\right)^3 dz\right.$$
$$\left. + \int_0^D \langle\rho_B(z)\rangle\left(\frac{\sigma}{D+z_0-z}\right)^3 dz\right]. \tag{31}$$

Other terms in the Hamiltonian being independent of ε_a, a derivative of F with respect to ε_a separates out

$$\left(\frac{\partial f_s^{z=0}}{\partial\varepsilon_a}\right)_T = \frac{2\pi\rho}{3}\int_0^D dz\left(\frac{\sigma}{z+z_0}\right)^3 \langle\rho_A(z)\rangle, \tag{32}$$
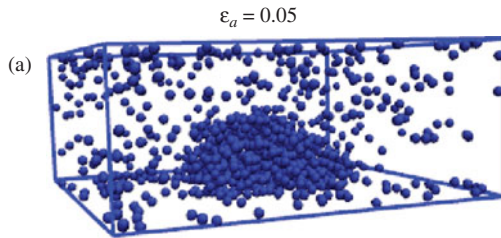
and

$$\left(\frac{\partial f_s^{z=D}}{\partial\varepsilon_a}\right)_T = \frac{2\pi\rho}{3}\int_0^D \left(\frac{\sigma}{D+z_0-z}\right)^3 \langle\rho_B(z)\rangle. \tag{33}$$

Upon integration, Equations (32) and (33) provide

$$f_s^{z=0}(\varepsilon_a) = f_s^{z=0}(0) + \left(\frac{2\pi\rho}{3}\right)$$
$$\times \int_0^{\varepsilon_a} d\varepsilon_a' \int_0^D dz \left(\frac{\sigma}{z+z_0}\right)^3 \langle\rho_A(\varepsilon_a', z)\rangle, \tag{34}$$

$$f_s^{z=D}(\varepsilon_a) = f_s^{z=D}(0) + \left(\frac{2\pi\rho}{3}\right)$$
$$\times \int_0^{\varepsilon_a} d\varepsilon_a' \int_0^D dz \left(\frac{\sigma}{D+z_0-z}\right)^3 \langle\rho_B(\varepsilon_a', z)\rangle. \tag{35}$$

From Equations (28), (34) and (35), we obtain

$$\gamma_{WA} - \gamma_{WB} = \left(\frac{2\pi\rho}{3}\right)\int_0^{\varepsilon_a} d\varepsilon_a' \int_0^D dz$$
$$\times \left[\langle\rho_A(\varepsilon_a', z)\rangle_{A-\text{rich}}\left(\frac{\sigma}{z+z_0}\right)^3\right.$$
$$\left. - \langle\rho_B(\varepsilon_a', z)\rangle_{A-\text{rich}}\left(\frac{\sigma}{D+z_0-z}\right)^3\right]. \tag{36}$$

By performing SGMC simulations at closely spaced values of $\varepsilon_a, \gamma_{WA} - \gamma_{WB}$ can be calculated rather accurately. Via the Young's equation, this will provide θ with the aid of γ calculated in previous subsection. A comparison of θ thus obtained (continuous line) with those from Figure 10 (symbols) is provided [83,84] in Figure 11(b). Even though, at this temperature the estimation from Figure 10 is not so difficult, at T close to T_c this method will provide unreasonable values. Of course, in both the methods, the value of D may play crucial roles in terms of finite-size effects. In the case of canonical simulations, there is expected to be strong size effects from L as well. This is due to interactions among AB interfaces leading to wetting transition at smaller ε_a. This, of course, can be corrected via appropriate finite-size scaling analysis. However, for the SGMC case no such interface along the direction perpendicular to the walls appear.

As in the bulk case, different wall-attached droplet structures, with varying size, can be obtained via umbrella sampling SGMC simulations in confinement. In Figure 12 (a), we show one such snapshot for a spherical or sphere-cap droplet.[83,84] Corresponding overall free energy density plot, analogous to the bulk case, this time only for a part of x_A range, is shown [84] in Figure 12(b). Extraction of interfacial contribution to the free energy is
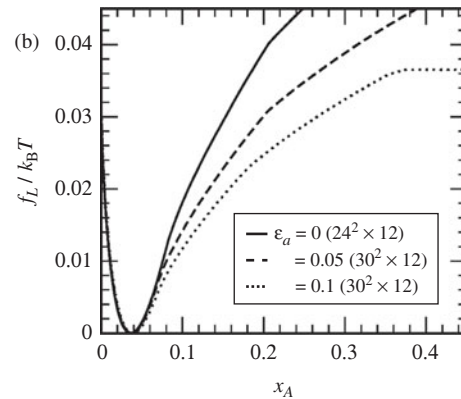
Figure 12. (Colour online) (a) Snapshot of an A-rich sphere-cap droplet for the fluid mixture confined between anti-symmetric walls. This was obtained from umbrella sampling SGMC simulation with $\varepsilon_a = 0.05$, $x_A = 0.12$, $D = 12$ and $L = 30$ at $T = 1$. Again, only A particles are shown. (b) Free energy densities, obtained from umbrella sampling SGMC simulations in $L^2 \times D$ boxes, are plotted versus x_A, at $T = 1$. The values of ε_a, L and D are mentioned on the figure. From Mol. Phys. **109**, 1043 (2011).

similar to the bulk case. Here, of course, we need to know that the volume of the sphere-cap droplet gets reduced, compared to the bulk droplet of same radius R, by a factor $f(\theta)$ given by [79]

$$f(\theta) = \frac{1}{4}(2 + \cos \theta)(1 - \cos \theta)^2. \qquad (37)$$

Results for interfacial free energy, F_s, from bulk and confinement, are shown in Figure 13. There the symbols represent simulation data for the variation of F_s, for wall-attached droplets at $T = 1$ for $\theta = 90°$, as a function of R. The corresponding plot for bulk spherical droplet at the same value of T is shown as well. Here we have also shown a theoretical curve using flat interfacial tension, as used in CNT, for bulk droplets. There is visible disagreement of the latter with the bulk simulation data, particularly for smaller values of R, due to curvature dependence of γ. In addition, the huge mismatch between the bulk and wall-attached droplets is certainly due to the difference in surface area in the two cases, for same droplet radius. For such heterogeneous nucleation, induced by wall, Turnbull pointed out that [79]

$$F_s(R, \theta) = 4\pi R^2 \gamma f(\theta). \qquad (38)$$

The dashed line in this figure is obtained after multiplying the bulk simulation data by $f(\theta)$ which certainly is very close to the symbols. The minor mismatch that still exists is due to the line tension, τ, that we introduce as [84]

$$F_S(R, \theta) = 4\pi R^2 \gamma(R)f(\theta) + 2\pi r \tau, \qquad (39)$$
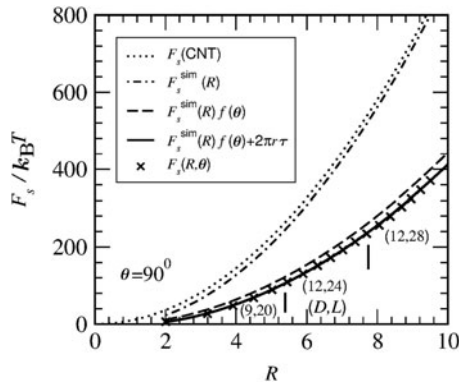
Figure 13.   Plot of various interfacial free energies as a function of droplet radii. The symbols correspond to simulation results for wall-attached droplets with contact angle 90°, i.e., $\varepsilon_a = 0$. The dashed-dotted line is for simulations of bulk droplets while the dotted line was obtained from CNT. The dashed line was obtained after multiplying the bulk simulation data by Turnbull factor. The continuous line, passing through the symbols, was obtained after making allowance for the line tension. For both bulk and confinement, the simulation results were obtained from umbrella sampling SGMC method. From Mol. Phys. **109**, 1043 (2011).
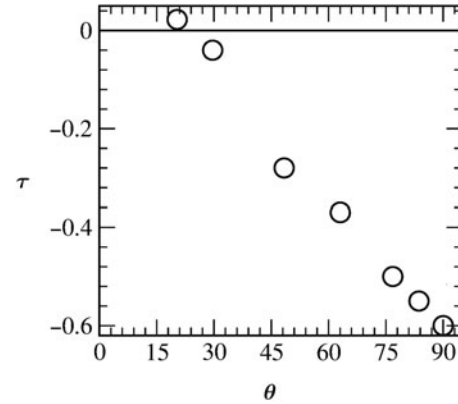
Figure 14.   Plot of line tension as a function of contact angle. From Mol. Phys. **109**, 1043 (2011).

where $r (= R \sin \theta)$ is the radius of the base of the wall-attached droplet.

The line tension can be obtained by treating it as an adjustable parameter to superimpose the bulk droplet data (continuous line in Figure 13) on the wall data. The values of τ, thus obtained,[84] are shown in Figure 14, for different values of ε_a, and so θ. The trend is similar to the density functional theoretical findings of Bauer and Dietrich [28], particularly the crossing of data from negative to positive values. Line tension can also be obtained from the free energies directly. This, for brevity, we do not discuss here.

Interfacial tensions can also be calculated via other computational methods. For example, another method, not discussed here, involves pressure tensors in MD simulations.[61,141]

3.   Kinetics of phase separation

When a homogeneous $A + B$ mixture is quenched inside the miscibility gap, it becomes unstable to fluctuations and evolves towards the coexisting equilibrium states via formation and growth of A- and B-rich domains. Typically, 'average' size, ℓ, of domains, during this growth, follows power law behaviour in time (t) as [1,33–39,55]

$$\ell(t) \sim t^\alpha. \qquad (40)$$

Here, we use the symbol ℓ, rather than R, to differentiate the length from equilibrium. The exponent α depends upon the number of order-parameter components, dimension d of the system and transport mechanism. Here, we confine ourselves to scalar order-parameter in $d = 2$ and 3. In the case of diffusive transport of material, only mechanism for phase separation in solid binary mixtures, we relate the interface velocity $d\ell/dt$ with the space gradient of chemical potential as [47]

$$\frac{\mathrm{d}\ell}{\mathrm{d}t} \sim |\vec{\nabla}\mu| \sim \frac{\gamma}{\ell^2}, \qquad (41)$$

to obtain $\alpha = 1/3$, referred to as the Lifshitz–Slyozov (LS) law [40]. For pure solid mixtures, on perfect lattice, we are expected to obtain this value for any composition (corresponding to nucleation or spinodal regime) [105] of A and B particles, at least asymptotically in time, irrespective of d.

The situation is significantly complex in fluid mixtures, because of the effects of hydrodynamics [36,41–45] at late stages of growth. There the dimensionality and composition influence the growth dynamics substantially. Let us first discuss the case with near critical (50:50) compositions, which has bicontinuous domain morphology.

At very early stage, of course, the LS law is expected due to the diffusive transport.[36] At a later time, depending upon thermodynamic and transport properties of the system, the diffusive mechanism becomes secondary to the faster hydrodynamic mechanism. In case of the latter, fast transport of material occurs through elongated tube-like domains due to pressure gradient that can be obtained from interfacial tension and average size of domains. The hydrodynamic growth regime is divided into two subregimes, namely viscous and inertial.

For the viscous hydrodynamic growth, a balance between the interfacial energy density and the viscous stress provides the interface velocity [36,43]

$$\frac{\mathrm{d}\ell}{\mathrm{d}t} \sim \frac{\gamma}{\eta}, \qquad (42)$$

η being the shear viscosity. Thus $\alpha = 1$. This picture holds for low Reynolds number, ℓ being in the range $(\lambda\eta)^{1/2} \le \ell \le \eta^2/\rho\gamma$, λ being a diffusion constant. For $\ell > \ell_{in} = \eta^2/\rho\gamma$, the kinetic energy density surpasses the viscous stress. In that case, a balance between the interfacial energy density and the kinetic energy density provides [36,44,45]

$$\frac{\mathrm{d}\ell}{\mathrm{d}t} \sim \left(\frac{\gamma}{\rho\ell}\right)^{1/2}, \qquad (43)$$

from which we obtain $\alpha = 2/3$.

In computer simulations, there exist results from the model H.[50,52] Even though some of these simulations observed both viscous and inertial regimes in $d = 3$, the situation in $d = 2$ is more controversial. MD simulations on the other hand are rare and more recent. [93,95,96,100,102–104]

For compositions close to the coexistence curves, the hydrodynamic mechanism described earlier does not hold. In this case, dynamics progresses via the nucleation and growth of droplets of the minority phase. As opposed to the solid binary mixtures, the motion of droplets in fluids is fast enough to provide a new mechanism via collision. Binder and Stauffer (BS) [41–43] proposed a Brownian droplet diffusion and collision mechanism. In that case, the droplet density, n, follows the differential equation

$$\frac{\mathrm{d}n}{\mathrm{d}t} = \lambda\ell n^2. \qquad (44)$$

Incorporating the Stokes–Einstein–Sutherland [128] relation and recognising that $n \propto 1/\ell^d$, from Equation (44) we find

$$\frac{\mathrm{d}\ell}{\mathrm{d}t} \sim \frac{1}{\ell^{d-1}}, \qquad (45)$$

solution of which provides $\alpha = 1/d$. Tanaka [51] pointed out that for high droplet density, the motion of droplets may not be random due to interdroplet interactions. This, however, only alters the amplitude of the growth. To the best of our knowledge, there exist no MD simulations for the droplet growth in binary fluid. However, MD simulations for the growth of liquid droplets in vapour–liquid transitions observed [106–108] $\alpha = 1/3$ in $d = 3$. Some preliminary studies [142] in $d = 2$ find $\alpha = 1/2$. These are certainly consistent with the prediction of BS. We do not discuss these results here, rather focus on the binary mixtures with critical composition.

Under confinement, depending upon the thickness of a film, it may be necessary to compare the results with the theoretical expectations in $d = 2$. This, however, is a priori unclear and is discussed later. As in equilibrium, here also we start with the bulk case to make the complexities appreciable in case of confinement.

3.1 Kinetics in bulk

With the objective of verifying the linear growth in the viscous hydrodynamic regime, MD simulations were performed for the bulk model [132,133] discussed in the previous section, using Nosé–Hoover thermostat (NHT). [126] The latter is known for its hydrodynamics preserving capability. Note that MC simulations, because of their stochastic nature, are not applicable for the studies of hydrodynamic phenomena. In these MD simulations, Verlet velocity algorithm,[126,127] with time step $\Delta t = 0.005t_{lj}$ (t_{lj} being the LJ time unit $= (m\sigma^2/\varepsilon)^{1/2}$ which we set to unity), was used to solve the equations of motion.

The objective [100,102] here is to observe the influence of hydrodynamics on domain growth. In MD simulations the ideal ensemble to study hydrodynamic effects is the constant NVE (E being the energy) or microcanonical ensemble. Equilibrium transport properties are traditionally calculated in this ensemble.[126,127] However, for studies of non-equilibrium evolution of systems, with temperature as a key parameter in the phase

behaviour, this ensemble is not suitable. This is because, as the system evolves by ordering, i.e., lowering its potential energy, only the increase of kinetic energy, i.e., of temperature will keep the total energy constant. Thus the system will eventually move outside the coexistence curve, invalidating the purpose of study. Thermostats are thus essential to keep the temperature constant.

There are various different thermostats that preserve the requirements of hydrodynamics rather well, namely NHT, dissipative particles dynamics (DPD),[143,144] etc. In this article, we present results only from MD simulations with NHT. This is because of its ability to keep temperature well under control, e.g., DPD thermostat, particularly in out-of-equilibrium situations, requires careful choices of parameters for well control over temperature.[145] Also, it is tested that for the type of systems we are addressing here, NHT produces results in equilibrium contexts, e.g., for transport properties, which are in extremely good agreement with *NVE* simulation results.[146] Before discussing the results, for the sake of completeness, we briefly describe the NHT in the following.

In this scheme, we solve the deterministic equations of motion for a particle at position $\vec{r}_i$ as

$$m_p \dot{\vec{r}}_i = \vec{p}_i, \qquad (46)$$

$$\dot{\vec{p}}_i = -\frac{\delta U}{\delta \vec{r}_i} - \Xi \vec{p}_i, \qquad (47)$$

$$\dot{\Xi} = \frac{\left(\sum_{i=1}^{N}(p_i^2/m_p) - 3Nk_BT\right)}{Q}. \qquad (48)$$

Here Ξ is a time-dependent drag and Q is a constant providing the strength of coupling between the system and the thermostat. The values of these quantities should be appropriately chosen for stability of the simulations. [126,143] The NHT is equivalent to a microcanonical ensemble with a modified Hamiltonian. The averages obtained from this method are equivalent to those from the canonical ensemble with the original Hamiltonian. [126,143]

We start by showing evolution snapshots,[100] at $T = 1.1$, from different times in Figure 15. It is clearly seen that the domains are interconnected in nature and growing with time. At small enough temperature the crossover from diffusive to hydrodynamic regime may get delayed. Thus, from the point of view of demanding nature of MD simulations, it is desirable to set the temperature at reasonably high value. This, however, comes with the difficulty in identifying domains due to the presence of thermal fluctuations over the scale of the equilibrium correlation length ξ. To avoid this problem, a majority particle rule [99] within a radius larger than ξ is employed
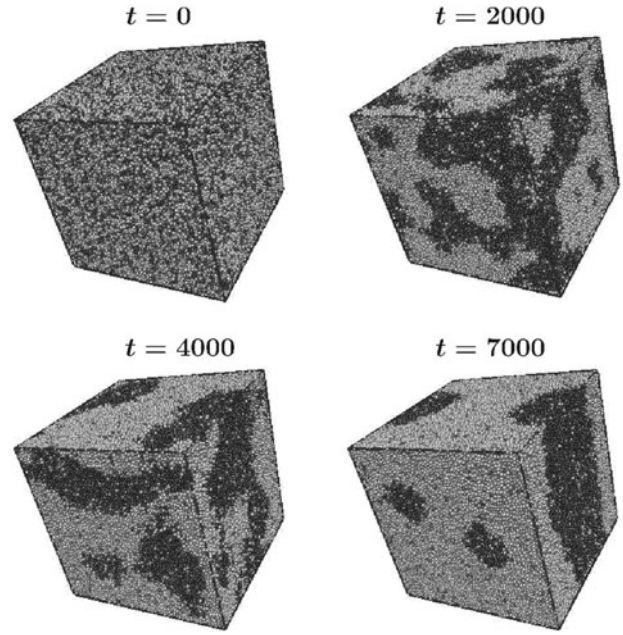

Figure 15.   Evolution snapshots of the bulk binary fluid having been quenched from homogeneously mixed state to $T = 1.1$. Various times are mentioned on top of the snapshots. The *A* particles are marked in black and *B* in grey. From Phys. Rev. E **82**, 040107 (2010).

to eliminate the noise to obtain a pure domain morphology. This method essentially coarse-grains the order parameter by averaging it over a length of order ξ.

The length scale from the above-mentioned pure domain morphology can be obtained from the decay of the two-point equal time correlation function [36]

$$C(r,t) = \frac{\langle \psi(0,t)\psi(\vec{r},t) \rangle}{\langle \psi(0,t)^2 \rangle}; \quad r = |\vec{r}|, \qquad (49)$$

this time the order parameter ψ is a local quantity and is defined in terms of $\rho_A(\vec{r},t)$ and $\rho_B(\vec{r},t)$, the local densities of *A* and *B* particles, as

$$\psi(\vec{r},t) = \frac{\rho_A(\vec{r},t) - \rho_B(\vec{r},t)}{\rho_A(\vec{r},t) + \rho_B(\vec{r},t)}. \qquad (50)$$

For the sake of convenience, this quantity is calculated only on the sites of an imaginary regular cubic lattice. In Figure 16(a), we plot [102] $C(r,t)$ from a few different times as a function of $r/\ell(t)$. Good collapse of data from all times on a master curve confirms the scaling property [36]

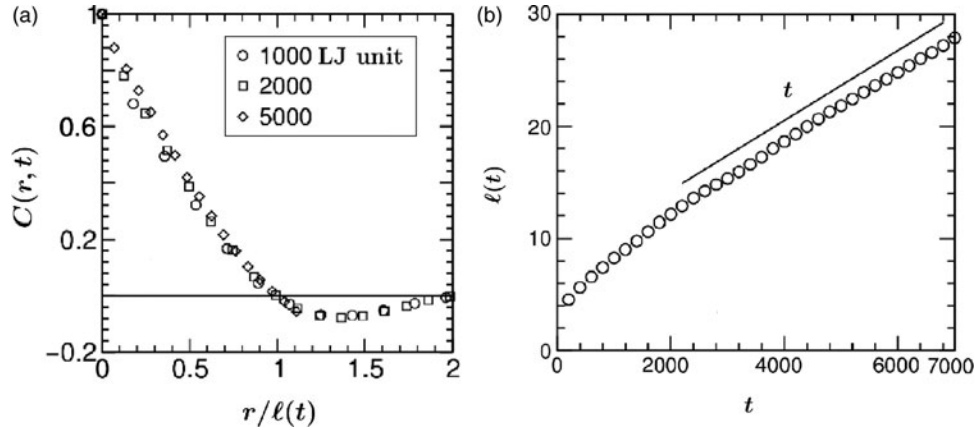$$C(r,t) \equiv \hat{C}\left(\frac{r}{\ell(t)}\right), \qquad (51)$$

Figure 16.   (a) Scaling plot of the two-point equal time correlation functions during the non-equilibrium evolution of the bulk binary fluid. Times are mentioned on the frame. (b) Plot of the average domain size, $\ell(t)$, as a function of time, for the evolution of the bulk binary fluid. The continuous straight line represents the viscous hydrodynamic behaviour. In both (a) and (b), the data were obtained from MD simulations at $T = 1.1$ with $L = 64$. From Phys. Rev. E **85**, 031140 (2012).

that stems from the self-similarity of domain patterns at different times, in a statistical sense.

A plot of $\ell(t)$, versus t, on linear scales, is shown [102] in Figure 16(b). Following an initial period of slower growth, a linear behaviour is visible, approximately after $t > 2000$. For accurate quantification of the exponent value in the faster growing regime, the following exercises are done.

A standard practice in numerical analysis of domain coarsening problems is to calculate the instantaneous exponent [47]

$$\alpha_i = \frac{d \ln \ell}{d \ln t}. \tag{52}$$

In Figure 17(a), a plot of α_i as a function of $1/\ell'$ ($\ell' = \ell - \ell_0$) is presented. Here ℓ_0 is a length related to

the crossover to the viscous hydrodynamic regime. Unless the length and time corresponding to a crossover, if present, is subtracted [99] from ℓ and t, we will obtain a much smaller value of α_i. In this plot, we have used the crossover time to be $t_0 = 2500$. For further clarification on this point, if a scaling regime, with exponent α, starts with non-zero length ℓ_0, at time t_0, we should write

$$\ell = \ell_0 + t_c^{\alpha}, \tag{53}$$

with $t_c = t - t_0$. Then [48,99]

$$\alpha_i = \alpha \left[1 - \frac{\ell_0}{\ell} \right]. \tag{54}$$

This linear behaviour of α_i, in $1/\ell$, has been a source of confusion and understood to be due to correction to α at
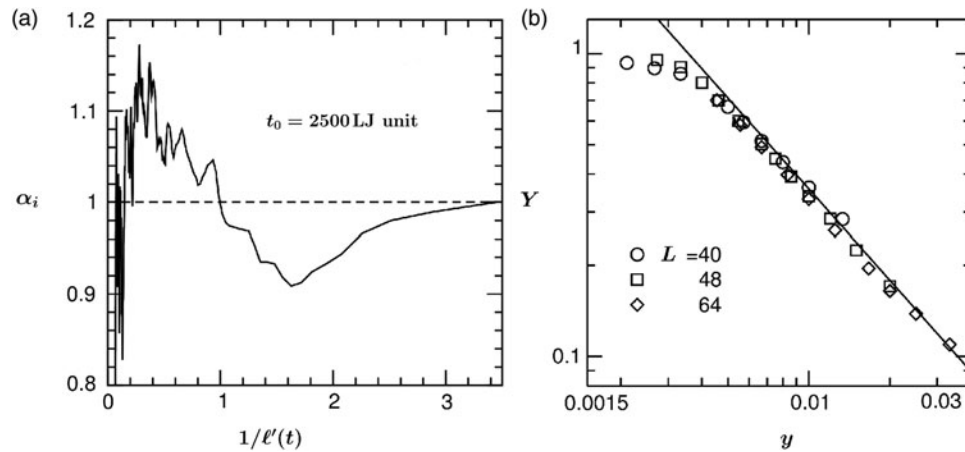

Figure 17.   (a) (From Phys. Rev. E **85**, 031140 (2012)) Instantaneous exponent α_i, for $L = 64$ at $T = 1.1$, is plotted versus $1/\ell'(t)$ with $\ell'(t) = \ell(t) - \ell(t_0)$; $t_0 = 2500$. (b) (From EPL **97**, 66006 (2012)) Finite-size scaling plot for domain growth in the bulk binary fluid. Data from three different system sizes have been used, as indicated on the figure. The continuous line represents a $1/y$ behaviour of the scaling function Y.

short time scales, in many computer simulations. But in many cases it appears, if ℓ_0 is subtracted from ℓ, $\alpha_i = \alpha$, independent of length. This provides a clearer way of understanding these simulation results. The values of t_0 or ℓ_0 can be quite accurately obtained, by treating one of them as an adjustable parameter, from finite-size data collapse experiments. Here, due to the linear behaviour in the post-crossover regime, any value of t_0 in that regime can be chosen. The oscillation of data around unity, in Figure 17(a), confirms the expectation in a viscous hydrodynamic regime.

Another method for identifying the growth exponents is the finite-size scaling analysis.[53,54,99] For the present (non-equilibrium) problem, this can be constructed in analogy with the equilibrium case by identifying $1/t$ with ϵ and ℓ with ξ. Then, for $X = \ell$, equation analogous to (12) is [104]

$$\ell = LY(y); \quad y = \frac{L^{1/\alpha}}{t}. \tag{55}$$

For $t \ll \infty$, the finite-size scaling function should obey

$$Y \sim y^{-\alpha}. \tag{56}$$

To work only with the scaling part in viscous hydrodynamic regime, here also we need to subtract ℓ_0 from all other lengths and counting of t must start from t_0. As stated earlier, any of these parameters (that will automatically fix the other), along with α, can be used as an adjustable quantity to obtain the data collapse. For $\ell_0 = 12$ ($t_0 = 2000$), finite-size scaling function, using data from few different sizes, is shown [104] as a function of y in Figure 17(b). For $\alpha = 1$, nice collapse of data, a requirement of the analysis, and decay of Y as $1/y$ for large y confirm this exponent. We, however, are unable to confirm the exponent in the inertial regime due to unavailability of resources that MD simulations demand. We are also unaware of any other MD study which achieved this objective.

3.2   Confinement

The phase separation kinetics in confined geometry is more complex because of the fascinating interplay between wetting and bulk phase separation.[56–60,80,110–124] Due to the constraints posed by the walls, the increase of domain length is restricted in the z-direction. Thus, if D is not large enough, meaningful quantitative analysis of ℓ can only be done in directions parallel to the walls. The latter should also be done with caution because of lack of material conservation in these xy planes, resulting from flow of the preferred particles towards the walls. Furthermore, as discussed already, the confinement reduces the critical temperature and coexistence curve gets distorted depending upon the wall–

particle interaction. We thus need to be careful about quenching a thin film inside the coexistence curve if only the knowledge of bulk coexistence curve is available.

To study the kinetics of fluid phase separation in thin films via MD simulations, we employ slightly different potentials. For particle–particle interactions, the force correction term is ignored, leading to a higher value [147] of bulk $T_c \simeq 1.638$. For wall–particle interactions, we have used [112,113]

$$u_s(z) = 32\pi\rho\sigma^3\varepsilon_w$$

$$\times \left[\frac{2}{15} \left(\frac{\sigma}{z + z_0} \right)^9 - \delta_s \left(\frac{\sigma}{D + z_0 - z} \right)^3 \right], \tag{57}$$

with $\varepsilon_w = 0.005$, $\delta_A = 1$ and $\delta_B = 0$. This implies a symmetric film, i.e., both the walls attract only A particles. All these simulations [112,113] were done at $T = 1.1$. The order-parameter at wall, discussed in the Introduction (see Figure 3), are from this model and temperature.

In Figures 18(a,b), we show evolution snapshots [112] for a film of thickness $D = 10$, starting from a homogeneous initial configuration of a 50:50 mixture. Only vertical (a) and horizontal (b) cross-sections are shown. Snapshots in (a) clearly show gradual wetting of walls by A particles. In that process, concentration of A particles in the bulk keeps decreasing. This is nicely quantified [112] in Figure 18(c) where we show the plots of order-parameter profiles, averaged over x and y coordinates, as a function of z. At early time, oscillatory profiles, providing information about alternating vertical regions (in z direction) rich and depleted in A particles, from both the walls propagate towards the centre of the film and collide. With time the walls get progressively more wet by A component whose depletion in the bulk thus further spreads, finally leaving a pronounced single minimum in the middle of the film. At the same time, as seen in the middle-layer snapshots in Figure 18(b), bulk phase separation continues. Pictures in Figure 18(b) provide information on the non-conservation of order parameter (in xy planes) with time. Thus, time regime for analysis of layer-wise growth of domains should be chosen carefully. The profiles in Figure 18(c) provide a fair idea about which time regime to consider meaningfully.

To quantify the layer-wise domain growth, we calculate the corresponding pair correlation functions. Here note that due to the composition asymmetry at layers, created by wetting at walls, we need to appropriately subtract the average value of the order parameter from the local value while calculating this quantity at various layers, so that for $r \to \infty$, $C(r, t) \to 0$.

In Figure 19, plots [112] of $\ell(t)$ versus t, for different layers in films of different thicknesses are shown. In all the cases, from these log–log plots it appears that
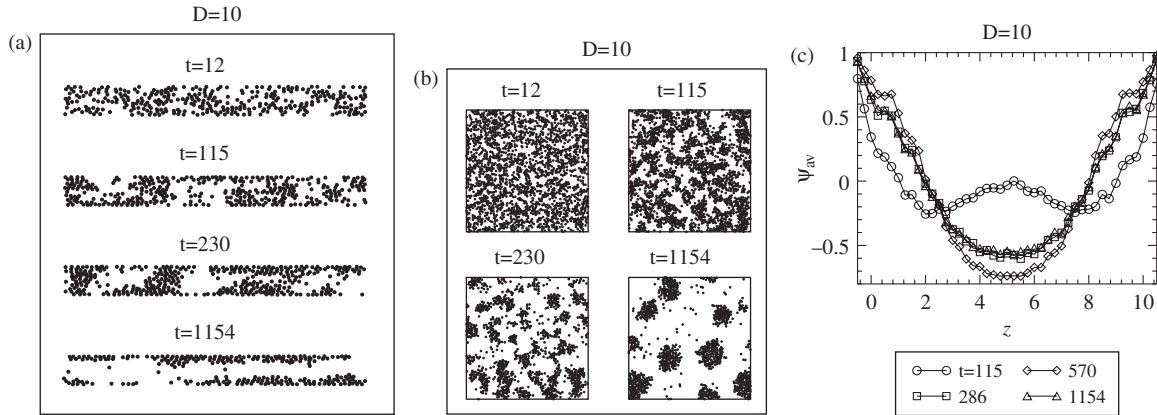
Figure 18.   (a) and (b): Vertical (*xz* plane) and horizontal (middle *xy* plane) cross-sections of evolution snapshots for a 50:50 binary LJ fluid confined between two symmetric parallel walls that prefer *A* particles. Only *A* particles are shown. (c) Layer-wise order-parameter profile is plotted versus *z* at different times. In all the cases, value of *D* is 10, with $L = 64$. From Phys. Rev. E **73**, 031604 (2006).

$$\ell(t) \sim t^{2/3}. \tag{58}$$

More recent simulations [124] of a different model, with multiparticle collision dynamics as hydrodynamics preserving apparatus, also provides similar conclusion for slip boundary conditions at the walls. This, however, is in contradiction with the expectation in viscous hydrodynamic regime. Here it should be recognised that for small enough *D*, the results should be referred to $d = 2$ case.

For $d = 2$, there is an alternative argument [46] about a crossover from $\alpha = 1/3$ to $1/2$, the latter coming from interface diffusion mechanism. For ultra thin films, this was observed in Ref. [124]. The simulation results presented in Figure 19 are at deviation from this expectation as well, even for $D = 5$. By looking at the snapshots in planes parallel to the walls, it may be misleadingly concluded that the growth should be via collision of droplets for which, again, in $d = 2$, $\alpha = 1/2$. But here these droplets are parts of columnar structures in *z*-direction, so a collision mechanism is unlikely. We, however, caution the reader that for accurate estimation of the exponent, more sophisticated analysis such as the finite-size scaling is needed. This, of course, requires data from varying *L* which are still missing.

In the case of thin films, the wetting layer cannot indefinitely grow. In semi-infinite geometry, however, thickness, R_1, of this layer can be very large. In that case, it is certainly meaningful to probe the time dependence of R_1. For the model described in the equilibrium context, this exercise was done [121,122] for two values of ε_a, as
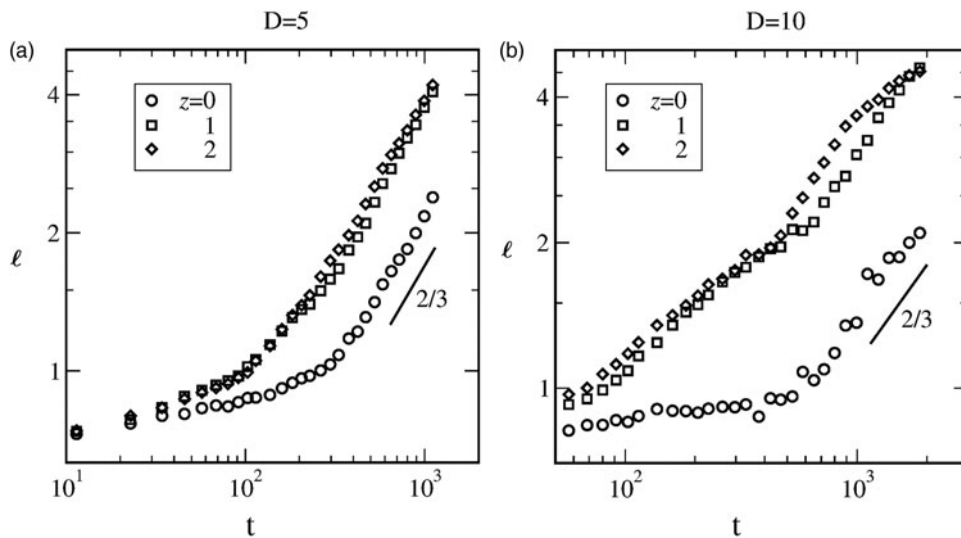

Figure 19.   Plots of $\ell(t)$ versus *t* for layer-wise domain growth in non-equilibrium films of thicknesses (a) $D = 5$ and (b) $D = 10$. The continuous lines represent power law growth with exponent 2/3. From Phys. Rev. E **73**, 031604 (2006).
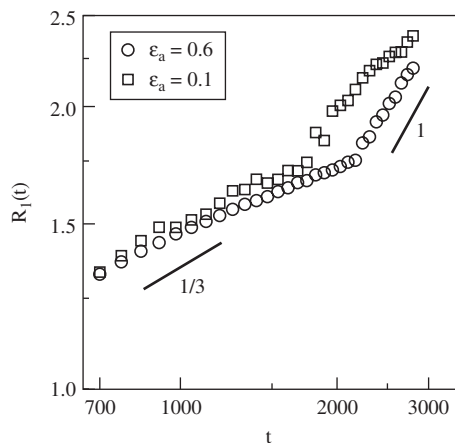
Figure 20.   Plot of thickness of the preferred particles at the wall during non-equilibrium evolution of a binary fluid in semi-infinite geometry. From Phys. Rev. E **85**, 051137 (2012).

seen in Figure 20, via MD simulations. There R_1 follows a $t^{1/3}$ diffusive growth at early time which crosses over to a linear hydrodynamic behaviour.

4.   Conclusion

In this article, we have reviewed some results for equilibrium and non-equilibrium properties of bulk and confined binary fluids in coexistence. Works [68–70,83,84,99,100,102,104,106–108,112,113,121,134,142] primarily discussed here are done with various collaborators with models having special symmetry.

In the equilibrium context, we have discussed MC methods and thermodynamic analysis techniques related to calculation of interfacial tension. Both flat and curved interfaces were considered. For the latter, an universal form for the bulk critical behaviour has been discussed which is expected to be valid irrespective of the model symmetry. On the non-equilibrium front, we have discussed various theoretical scenarios for the kinetics of fluid-phase separation. MD simulations results are presented as verification of these pictures.

In light of the discussion and results on bulk systems, complexity of problems and corresponding computational difficulties under confinement are pointed out. Among the methodologies to tackle these issues, we have presented a thermodynamic method for obtaining contact angle. This is advantageous compared to traditional geometrical method, particularly at higher temperatures. Results for wetting phenomena, using this method, have been presented. In this context, line tension has been introduced. For the kinetics of phase separation, contrasting results for the hydrodynamic growth with that of bulk is discussed. Due to the interplay between wetting at wall and phase separation in the bulk, the kinetics is very rich

and poses challenge in quantification of growth, particularly via MD simulations.

Even though the discussions have more general validity, the results are presented only from the simulations of a symmetric binary LJ model. This model is a unique one for which a large number of bulk properties, e.g., phase diagram, static and dynamic critical behaviour, and coarsening dynamics, have been understood with relative ease. In the confinement problem, wetting properties, including contact angle and line tension, have been extracted via state-of-the-art simulation methods. This model is thus a unique 'laboratory' for testing analytical methods such as classical density functional and integral equation theories of fluids. It is hoped that this will stay useful in the future. To highlight the usefulness of the model further, before closing, we briefly discuss the kinetics of phase transition with quenched disorder.

Systems with quenched disorder are of obvious experimental importance and relevant to studies related to porous media and thus confinement. Kinetics of phase separation in disordered Ising models received significant importance. There it has been established [148] that disorder brings in a crossover in the domain growth law, from a power law behaviour to a logarithmic behaviour. Such studies in fluids, particularly via MD simulations, were lacking, due to obvious difficulty. However, recently it has been demonstrated that, if a model is appropriately chosen, such as the present binary LJ, MD simulations can be fruitfully performed to understand the effects of disorder in fluids. The outcome of this study [149] appears to be very similar to the disordered Ising models, as far as growth of domains is concerned.

Disclosure statement

No potential conflict of interest was reported by the author.

References

[1] Onuki A. Phase transition dynamics. Cambridge: Cambridge University Press; 2002.

[2] Fisher ME. Theory of equilibrium critical phenomena. Rep Prog Phys. 1967;30:615−730.

[3] Kadanoff LP, Gotze W, Hamblen D, Hecht R, Lewis EAS, Palciauskas VV, Rayl M, Swift J, Aspnes D, Kane J. Static phenomena near critical points: theory and experiment. Rev Mod Phys. 1967;39:395−431.

[4] Wilson KG. The renormalization group: critical phenomena and the Kondo problem. Rev Mod Phys. 1995;47:773−840.

[5] Fisher ME. The renormalization group in the theory of critical behavior. Rev Mod Phys. 1975;46:597−616.

[6] Stanley HE. Introduction to phase transitions and critical phenomena. Oxford: Oxford University Press; 1971.

[7] Binder K. Theory of first-order phase transitions. Rep Prog Phys. 1987;50:783−859.

[8] Privman V, Hohenberg PC, Aharony A. Universal critical-point amplitude ratios. In: Domb C, Lebowitz JL, editors. Phase transitions and critical phenomena. Vol. 14. New York, NY: Academic. Chapter 1 1991. p. 1−134.

[9] Binder K, Luijten E. Monte Carlo tests of renormalization group predictions for critical phenomena in Ising Models. Phys Rep. 2001;344:179−253.

[10] Abraham FF. Homogeneous nucleation theory. New York, NY: Academic; 1974.

[11] Evans R. The nature of the liquid−vapor interface and other topics in the statistical mechanics of non-uniform, classical fluids. Adv Phys. 1979;28:143−200.

[12] Furukawa H, Binder K. Two-phase equilibria and nucleation barriers near a critical point. Phys Rev A. 1982;26:556−566.

[13] Sullivan DE, Telo da Gamma MM, In: Croxton CA, editor. Fluid interfacial phenomena. New York, NY: Wiley; 1986. p. 45−134.

[14] Dietrich S. Wetting phenomena. In: Domb C, Lebowitz JL, editors. Phase transitions and critical phenomena. London: Academic Press. Chapter 1. 1988. p. 1.

[15] Hendersen D. Fundamentals of inhomogeneous fluids. New York, NY: M. Dekker; 1992.

[16] Oxtoby DW. Homogeneous nucleation: theory and experiment. J Phys: Condens Matter. 1992;4:7627−7650.

[17] Rowlinson JS, Widom B. Molecular theory of capilarity. Oxford: Clarendon; 1982.

[18] ten Wolde PR, Frankel D. Computer simulation study of gas−liquid nucleation in a Lennard-Jones system. J Chem Phys. 1998;109:9901−9918.

[19] Kashchiev D. Nucleation: basic theory with applications. Oxford: Butterworth-Heinemann; 2000.

[20] Nussbaumer A, Bittner E, Janke W. Evaporation/condensation of Ising droplets. Proceedings of Science. 2005:252.

[21] Fisher ME, Nakanishi H. Scaling theory for the criticality of fluids between plates. J Chem Phys. 1981;75:5857−5863.

[22] de Gennes PG. Wetting: statics and dynamics. Rev Mod Phys. 1985;57:827−863.

[23] Evans R. Fluids adsorbed in narrow pores: phase equilibria and structure. J Phys: Condens Matter. 1990;2:8989−9007.

[24] Parry AO, Evans R. Influence of wetting on phase equilibria: a novel mechanism for critical point shifts in films. Phys Rev Lett. 1990;64:439−442.

[25] Swift MR, Owczarek AL, Indekeu JO. Effect of confinement on wetting and drying between opposing boundaries. Europhys, Lett. 1991;14:475−481.

[26] Binder K, Evans R, Landau DP, Ferrenberg AM. Interface localization transition in Ising films with competing walls: Ginzburg criterion and crossover scaling. Phys Rev E. 1996;53:5023−5034.

[27] Getta T, Dietrich S. Line tension between fluid phases and a substrate. Phys Rev E. 1998;57:655−671.

[28] Bauer C, Dietrich S. Quantitative study of laterally inhomogeneous wetting films. Eur Phys J B. 1999;10:767−779.

[29] Valencia A, Brinkmann M, Lipowsky R. Liquid bridges in chemically structured slit pores. Langmuir. 2001;17:3390−3399.

[30] de Gennes PG, Brochard-Wyart F, Quéle D. Capilarity and wetting phenomena: drops, bubbles, pearls. Berlin: Springer; 2004.

[31] Albano EV, Binder K. Phase coexistence in nanoscopically thin films confined by asymmetric walls. J Stat Phys. 2009;135:991−1008.

[32] Cross MC, Hohenberg PC. Pattern formation outside of equilibrium. Rev Mod Phys. 1993;65:851.

[33] Jones RAL. Soft condensed matter. Oxford: Oxford University Press; 2002.

[34] Komura S, Furukawa H, editors. Dynamics of ordering processes in condensed matter. New York, NY: Plenum Press; 1988.

[35] Binder K. Spinodal decomposition. In: Cahn RW, Haasen P, Kramer EJ, editors. Materials science and technology. Vol. 5: Phase transformation of materials Weinheim: VCH; 1991. p. 405−471.

[36] Bray AJ. Theory of phase ordering kinetics. Adv Phys. 2002;51:481−587.

[37] Dattagupta S, Puri S. Dissipative phenomena in condensed matter: some applications. Heidelberg: Springer; 2004.

[38] Puri S. Surface directed spinodal decomposition. J Phys: Condens Matter. 2005;17:R101−R142.

[39] Puri S, Wadhawan V, editors. Kinetics of phase transitions. Boca Raton, FL: CRC Press; 2009.

[40] Lifshitz IM, Slyozov VV. The kinetics of precipitation from supersaturated solid solutions. J Phys Chem Solids. 1961;19:35−50.

[41] Binder K, Stauffer D. Theory for the slowing down of the relaxation and spinodal decomposition of binary mixtures. Phys, Rev, Lett. 1974;33:1006−1009.

[42] Binder K. Theory of the dynamics of 'Clusters' II. Critical diffusion in binary systems and the kinetics of phase separation. Phys Rev B. 1977;15:4425−4447.

[43] Siggia ED. Late stages of spinodal decomposition in binary mixtures. Phys Rev A. 1979;20:595−605.

[44] Furukawa H. Effect of inertia on droplet growth in a fluid. Phys Rev A. 1985;31:1103−1108.

[45] Furukawa H. Turbulent growth of percolated droplets in phase separating fluids. Phys Rev A. 1987;36:2288−2292.

[46] San Miguel M, Grant M, Gunton JD. Phase separation in two-dimensional binary fluids. Phys Rev A. 1985;31:1001−1005.

[47] Huse DA. Corrections to late-stage behavior in spinodal decomposition: Lifshitz−Slyozov scaling and Monte Carlo simulations. Phys Rev B. 1986;34:7845−7850.

[48] Amar JG, Sullivan FE, Mountain RD. Monte Carlo study of growth in the two-dimensional spin-exchange kinetic Ising model. Phys Rev B. 1988;37:196−208.

[49] Marko JF, Barkema GT. Phase ordering in the Ising model with conserved spin. Phys Rev E. 1995;52:2522−2534.

[50] Puri S, Dünweg B. Temporally linear domain growth in the segregation of binary fluids. Phys Rev A. 1992;45:R6977−R6980.

[51] Tanaka H. New mechanisms of droplet coarsening in phase-separating fluid mixtures. J Chem Phys. 1997;107:3734−3737.

[52] Kendon VM, Cates ME, Pagonabarraga I, Desplat JC, Blandon P. Inertial effects in three-dimensional spinodal decomposition of a symmetric binary fluid mixture: a lattice Boltzmann study. J Fluid Mech. 2001;440:147−203.

[53] Heermann DW, Yixue L, Binder K. Scaling solutions and finite-size effects in the Lifshitz−Slyozov theory. Physica A. 1996;230:132−148.

[54] Vinals J, Jasnow D. Finite-size scaling analysis of domain growth in the kinetic Ising model with conserved and nonconserved order parameters. Phys Rev B. 1998;37:9582−9589.

[55] Binder K, Puri S, Das SK, Horbach J. Phase separation in confined geometries. J Stat Phys. 2010;138:51−84.

[56] Jones RAL, Norton LJ, Kramer EJ, Bates FS, Wiltzius P. Surface directed spinodal decomposition. Phys Rev Lett. 1991;66:1326−1329.

[57] Brown G, Chakrabarti A. Surface directed spinodal decomposition in a two-dimensional model. Phys Rev A. 1992;46:4829−4835.

[58] Puri S, Binder K. Surface directed spinodal decomposition: phenomenology and numerical results. Phys Rev A. 1992;46:R4487−R4489.

[59] Puri S, Binder K. Surface effects on spinodal decomposition in binary mixtures and the interplay with wetting phenomena. Phys Rev E. 1994;49:5359−5377.

[60] Puri S, Frisch HL. Surface directed spinodal decomposition: modelling and numerical simulations. J Phys: Condens Matter. 1997;9:2109−2133.

[61] Nicolas JP, Smit B. Molecular dynamics simulations of the surface tension of *n*-hexane, *n*-decane and *n*-hexadecane. Mol Phys. 2002; 100:2471–2475.

[62] Vink RLC, Horbach J, Binder K. Critical phenomena in colloid–polymer mixtures: interfacial tension, order parameter, susceptibility and coexistence diameter. Phys Rev E. 2005;71:011401.

[63] Anisimov MA. Divergence of Tolman length for a droplet near the critical point. Phys Rev Lett. 2007;98:035702.

[64] Schrader M, Virnau P, Binder K. Simulation of vapor–liquid coexistence in finite volumes: a method to compute the surface free energy of droplets. Phys Rev E. 2009;79:061104.

[65] Tröster A, Binder K. Microcanonical determination of the interface tension of flat and curved interfaces from Monte Carlo simulations. J Phys: Condens Matter. 2012;24:284107.

[66] Prestipino S, Laio A, Tosatti E. A fingerprint of surface-tension anisotropy in the free energy cost of nucleation. J Chem Phys. 2013;138:064508.

[67] Blokhuis EM, van Giessen AE. Density functional theory of a curved liquid–vapor interface: evaluation of the rigidity constants. J Phys: Condens Matter. 2013;25:225003.

[68] Block BJ, Das SK, Oettel M, Virnau P, Binder K. Curvature dependence of surface free energy of liquid drops and bubbles: a simulation study. J Chem Phys. 2010;133:154702.

[69] Das SK, Binder K. Thermodynamic properties of a symmetrical binary mixture in the coexistence region. Phys Rev E. 2011;84: 061607.

[70] Das SK, Binder K. Universal critical behavior of curvature dependent interfacial tension. Phys Rev Lett. 2011;107:235702.

[71] Calvo F. Molecular dynamics determination of surface tension of silver–gold liquid alloys and the Tolman length of nanoalloys. J Chem Phys. 2012;136:154701.

[72] Horsch M, Hasse H. Molecular simulation of nano-dispersed fluid phases. Chem Eng Sci. 2014;107:235–244.

[73] Rocha FM, Miranda JA. Manipulation of the Saffman-Taylor instability: a curvature-dependent surface tension approach. Phys Rev E. 2013;87:013017.

[74] Zhukhovitskii DI. Molecular dynamics study of nanobubbles in the equilibrium Lennard-Jones fluid. J Chem Phys. 2013;139: 164513.

[75] Horsch M, Hasse H, Shchekin AK, Agarwal A, Eckelsbach S, Vrabec J, Müller EA, Jackson G. Excess equimolar radius of liquid drops. Phys Rev E. 2012;85:031605.

[76] Bertrand CE, Anisimov MA. Complete scaling of inhomogeneous fluids. Phys Rev Lett. 2012;104:205702.

[77] Anisimov MA, St. Pierre HJ. Diverging curvature correction to the interfacial tension in polymer solutions. Phys Rev E. 2008;78: 011105.

[78] Benjamin R, Horbach J. Crystal–liquid interfacial free energy via thermodynamic integration. J Chem Phys. 2014;141:044715.

[79] Binder K, Block BJ, Das SK, Virnau P, Winter D. Monte Carlo methods for estimating interfacial free energies and line tensions. J Stat Phys. 2011;144:690–729.

[80] Tanaka H. Interplay between wetting and phase separation in binary fluid mixtures: roles of hydrodynamics. J Phys: Condens Matter. 2001;13:4637–4674.

[81] Winter D, Virnau P, Binder K. Monte Carlo test of the classical theory of heterogeneous nucleation barriers. Phys Rev Lett. 2009; 103:225703.

[82] Winter D, Virnau P, Binder K. Heterogeneous nucleation at a wall near a wetting transition: a Monte Carlo test of the classical theory. J Phys: Condens Matter. 2009;21:464118.

[83] Das SK, Binder K. Does Young's equation hold on the nanoscale? A Monte Carlo test for the binary Lennard-Jones fluid. EPL. 2010; 92:26006.

[84] Das SK, Binder K. Simulation of binary fluids exposed to selectively adsorbing walls: a method to estimate contact angles and line tensions. Mol Phys. 2011;109:1043–1056.

[85] Peng H, Birkett GR, Aguyen AV. The impact of line tension on the contact angle of nanodroplets. Mol Simul. 2014;40:934–941.

[86] Deb D, Winkler A, Virnau P, Binder K. Simulation of fluid–solid coexistence in finite volumes: a method to study properties of wall-attached crystalline nuclei. J Chem Phys. 2012;136:134710.

[87] Kumar V, Errington JR. Understanding wetting of immiscible liquids near a solid surface using molecular simulation. J Chem Phys. 2013;139:064110.

[88] Seveno D, Blake TD, Coninck JD. Young's equation at the nanoscale. Phys Rev Lett. 2013;111:096101.

[89] Zhou D, Zhang F, Mi J, Zhong C. Line tension and contact angle of heterogeneous nucleation of binary fluids. AIChE J. 2013;59: 4390–4398.

[90] Laird BB, Hunter A, Davidchack RL. Interfacial free energy of a hard-sphere fluid in contact with curved surfaces. Phys Rev E. 2012;86:060602.

[91] Schmitz F, Virnau P, Binder K. Determination of the origin and magnitude of logarithmic finite-size effects on interfacial tension: role of interfacial fluctuations and domain breathing. Phys Rev Lett. 2014;112:239902.

[92] Schmitz F, Virnau P, Binder K. Logarithmic finite-size effects on interfacial free energies: phenomenological theory and Monte Carlo studies. Phys, Rev, E. 2014;90:012128.

[93] Laradji M, Toxvaerd S, Mountain OG. Molecular dynamics simulation of spinodal decomposition in three-dimensional binary fluids. Phys Rev Lett. 1996;77:2253–2256.

[94] Mitchel SJ, Landau DP. Phase separation in a compressible 2D Ising model. Phys Rev Lett. 2006;97:025701.

[95] Kabrede H, Hentschke R. Spinodal decomposition in a 3D Lennard-Jones system. Phys A. 2006;361:485–493.

[96] Thakre AK, den Otte WK, Briels WJ. Domain formation and growth in spinodal decomposition of a binary fluid by molecular dynamics simulations. Phys Rev E. 2008;77:011503.

[97] Corberi F, Lippiello E, Zannetti M. Interface fluctuations, bulk fluctuations, and dimensionality in the off-equilibrium response of coarsening systems. Phys Rev E. 2001;63:061506.

[98] Corberi F, Lippiello E, Zannetti M. Influence of thermal fluctuations on the geometry of interfaces of the quenched Ising model. Phys, Rev, E.. 2008;78:011109.

[99] Majumder S, Das SK. Domain coarsening in two dimensions: conserved dynamics and finite-size scaling. Phys Rev E. 2010;81: 050102.

[100] Ahmad S, Das SK, Puri S. Kinetics of phase separation in fluids: a molecular dynamics study. Phys Rev E. 2010;82:040107.

[101] Majumder S, Das SK. Diffusive domain coarsening: early time dynamics and finite-size effects. Phys Rev E. 2011;84:021110.

[102] Ahmad S, Das SK, Puri S. Crossover in growth laws for phase separating binary fluids: molecular dynamics simulations. Phys Rev E. 2012;85:031140.

[103] Majumder S, Das SK. Universality in fluid domain coarsening: the case of vapor–liquid transition. EPL. 2011;95:46002.

[104] Das SK, Roy S, Majumder S, Ahmad S. Finite-size effects in dynamics: critical versus coarsening phenomena. EPL. 2012;97: 66006.

[105] Majumder S, Das SK. Temperature and composition dependence of kinetics of phase separation in solid binary mixtures. Phys, Chem, Chem, Phys. 2013;15:13209–13218.

[106] Roy S, Das SK. Nucleation and growth of droplets in vapor–liquid transitions. Phys Rev E. 2012;85:050602.

[107] Roy S, Das SK. Dynamics and growth of droplets close to the coexistence curve in fluids. Soft Matter. 2013;9:4178–4187.

[108] Roy S, Das SK. Effects of domain morphology on kinetics of fluid phase separation. J Chem Phys. 2013;139:044911.

[109] Yelash L, Virnau P, Paul W, Binder K, Muller M. Spinodal decomposition of polymer solutions: a parallelized molecular dynamics simulation. Phys Rev E. 2008;78:031801.

[110] Bastea S, Puri S, Lebowitz JL. Surface directed spinodal decomposition in binary fluid mixtures. Phys Rev E. 2001;63:041513.

[111] Das SK, Puri S, Horbach J, Binder K. Kinetics of phase separation in thin films: simulations for the diffusive case. Phys Rev E. 2005; 72:061603.

[112] Das SK, Puri S, Horbach J, Binder K. Spinodal decomposition in thin films: molecular dynamics simulations of a binary Lennard-Jones fluid mixture. Phys Rev E. 2006;73:031604.

[113] Das SK, Puri S, Horbach J, Binder K. Molecular dynamics study of phase separation kinetics in thin films. Phys Rev Lett. 2006;96: 016107.

[114] Yan L-T, Li J, Xie X-M. Three dimensional numerical simulations of lamellar structure via two-step surface-directed phase separation in polymer blend films. J Chem Phys. 2008;128: 224906.

[115] Das SK, Horbach J, Binder K. Kinetics of phase separation in thin films. Lattice versus continuum models for solid binary mixtures. Phys Rev E. 2009;79:021602.

[116] Xu Z, Hao Z, Ni J, Iwata S. Path of ordering under confinement in alloy films. Thin Solid Films. 2009;517:1848–1852.

[117] Liu J, Wu X, Lennard WN, Landheer D. Surface-directed spinodal decomposition in hafnium silicate thin films. Phys Rev B. 2009;80: 041403.

[118] Bucior K, Yelash L, Binder K. Phase separation of an asymmetric binary-fluid mixture confined in a nanoscopic slit pore: molecular dynamics simulations. Phys Rev E. 2008;77:051602.

[119] Bucior K, Yelash L, Binder K. Molecular dynamics simulation of evaporation processes of fluid bridges confined in slit-like pores. Phys Rev E. 2009;79:031604.

[120] Hore MJA, Laradji M. Dissipative particle dynamics simulation of the interplay between spinodal decomposition and wetting in thin film binary fluids. J Chem Phys. 2010;132:024908.

[121] Jaiswal PK, Puri S, Das SK. Surface directed spinodal decomposition: a molecular dynamics study. Phys Rev E. 2012;85:051137.

[122] Jaiswal PK, Puri S, Das SK. Hydrodynamic crossovers in surface directed spinodal decomposition and surface enrichment. Europhys Lett. 2012;97:16005-P1–16005-P5.

[123] Jamie EAG, Dullens RPA, Aarts DGAL. Spinodal decomposition of a confined colloid–polymer system. J Chem Phys. 2012;137:204902.

[124] Winkler A, Virnau P, Binder K, Winkler RG, Gompper G. Hydrodynamic mechanisms of spinodal decomposition in confined colloid–polymer mixtures: a multiparticle collision dynamics study. J Chem Phys. 2013;138:054901.

[125] Landau DP, Binder K. A guide to Monte Carlo simulations in statistical physics. Cambridge: Cambridge University Press; 2009.

[126] Frenkel D, Smit B. Understanding molecular simulations: from algorithm to applications. San Diego: Academic Press; 2002.

[127] Allen MP, Tildesley DJ. Computer simulations of liquids. Oxford: Clarendon; 1987.

[128] Hansen JP, McDonald IR. Theory of simple liquids. London: Academic; 1986.

[129] Fisher ME. In: Green MS, editor. Critical Phenomena. London: Academic Press; 1971. p. 1.

[130] Fisher ME, Barber MN. Scaling theory for finite-size effects in the critical region. Phys Rev Lett. 1972;28:1516–1519.

[131] Privman V, editor. Finite-size scaling and numerical simulation of statistical systems. Singapore: World Scientific; 1990.

[132] Das SK, Horbach J, Binder K, Fisher ME, Sengers JV. Static and dynamic critical behavior of a symmetrical binary fluid: a computer simulation. J Chem Phys. 2006;125:024506.

[133] Das SK, Fisher ME, Sengers JV, Horbach J, Binder K. Critical dynamics in a binary fluid: simulations and finite-size scaling. Phys Rev Lett. 2006;97:025702.

[134] Roy S, Das SK. Transport phenomena in fluids: finite-size scaling for critical behavior. EPL. 2011;94:36001-P1–36001-P6.

[135] Roy S, Das SK. Simulation of transport around the coexistence region of a binary fluid. J Chem Phys. 2013;139:064505.

[136] Virnau P, Muller M. Calculation of free energy through successive umbrella sampling. J Chem Phys. 2004;120:10925–10930.

[137] Fisher MPA, Wortis M. Curvature corrections to the surface tension of fluid drops: Landau theory and a scaling hypothesis. Phys Rev B. 1984;29:6252–6260.

[138] Tolman RC. Consideration of the Gibbs theory of surface tension. J Chem Phys. 1948;16:758–774.

[139] Tolman RC. The supercritical density of matter at a liquid–vapor boundary. J Chem Phys. 1949;17:118–127.

[140] Tolman RC. The effect of droplet size on surface tension. J Chem Phys. 1949;17:333–337.

[141] Alejandre J, Tildesley DJ, Chapela GA. Fluid phase equilibria using molecular dynamics: the surface tension of chlorine and hexane. Mol Phys. 1995;85:651–663.

[142] Midya J, Das SK. To be published.

[143] Stoyanov SD, Groot RD. From molecular dynamics to hydrodynamics: a novel Galilean invariant thermostat. J Chem Phys. 2005;122:114112.

[144] Nikunen P, Karttunen M, Vattulainen I. How would you integrate the equations of motion in dissipative particle dynamics simulations? Comp. Phys Comp.. 2003;153:407–423.

[145] Pastorino C, Kreer T, Mller M, Binder K. Comparison of dissipative particle dynamics and Langevin thermostats for out-of-equilibrium simulations of polymeric systems. Phys Rev E. 2007;76:026706.

[146] Roy S, Das SK. Finite-size scaling study of shear viscosity anomaly at liquid–liquid criticality. J Chem Phys. 2014;141: 234502-1–234502-6.

[147] Das SK, Horbach J, Binder K. Transport phenomena and microscopic structure in partially miscible binary fluids: a simulation study of the symmetrical Lennard-Jones mixture. J Chem Phys. 2003;119:1547–1558.

[148] Corberi F, Lippiello E, Mukherjee A, Puri S, Zannetti M. Growth law and superuniversality in the coarsening of disordered ferromagnets. J Stat Mech. 2011 :P03016.

[149] Ahmad S, Puri S, Das SK. Phase separation of fluids in porous media: a molecular dynamics study. Phys Rev E. 2014;90:040302(R).